C. T.-C. Nguyen, "Transceiver front-end architectures using vibrating micromechanical signal processors," chapter in *RF Technologies for Low Power Wireless Communications*, edited by G. I. Haddad, T. Itoh, and J. Harvey, pp. 411-461. New York: Wiley IEEE-Press, 2001. (50 pages)

Transceiver Front-End Architectures Using Vibrating Micromechanical Signal Processors

Clark T.-C. Nguyen

Center for Integrated Microsystems
Department of Electrical Engineering and Computer Science
University of Michigan
Ann Arbor, Michigan 48109-2122

Abstract—**The design of mechanical circuits based upon micromechanical vibrating beam elements is reviewed with a focus on the circuits most useful for communications applications. Communication transceiver architectures are then proposed that best harness the tiny size, zero dc power dissipation, and ultra-high-*Q* of vibrating micromechanical resonator circuits. Among the more aggressive architectures proposed are one based on a micromechanical RF channel-selector and one featuring an all-MEMS RF front-end. These architectures maximize performance gains by using highly selective, low-loss micromechanical circuits on a massive scale, taking full advantage of *Q* versus power trade-offs. Micromechanical filters, mixer-filters, and switchable synthesizers are identified as key blocks capable of substantial power savings when used in the aforementioned architectures. As a result of this architectural exercise, more focused directions for further research and development in RF MEMS are identified.**

1. Introduction

The need for passive off-chip components has long been a key barrier against communication transceiver miniaturization. In particular, the majority of the high-*Q* bandpass filters commonly used in the RF and IF stages of heterodyning transceivers are realized using off-chip, mechanically-resonant components, such as crystal filters and SAW devices. Due to higher quality factor *Q*, such technologies greatly outperform comparable filters implemented using transistor technologies, in insertion loss, percent bandwidth, and achievable rejection [1]-[8]. High *Q* is further required to implement local oscillators or synchronizing clocks in transceivers, both of which must satisfy strict phase noise specifications. Again, off-chip elements (e.g., quartz crystals) are utilized for this purpose. Being off-chip components, the above mechanical devices must interface with integrated electronics at the board level, and this constitutes an important bottleneck against the miniaturization of super-heterodyne transceivers. For this reason, recent attempts to achieve single-chip transceivers for paging and cellular communications have utilized alternative architectures [9], [10], that attempt to eliminate the need for off-chip high-*Q* components via higher levels of transistor integration. Unfortunately, without adequate front-end selectivity, such approaches have suffered somewhat in overall performance, to the point where they so far are usable only in less demanding applications. Given this, and recognizing that future communication needs will most likely require higher levels of performance, single-chip transceiver solutions that retain high-*Q* components and that preserve super-heterodyne-like architectures are desirable.

Recent demonstrations of vibrating beam micromechanical ("∝mechanical") resonator devices with frequencies in the VHF range and *Q*'s in the tens of thousands [11], [12] have sparked a resurgence of research interest in communication architectures using high-*Q* passive devices. Much of the interest in these devices derives from their use of IC-compatible microelectromechanical systems (MEMS) fabrication technologies [8], [13] to greatly facilitate the on-chip integration of ultra-high-*Q* passive tanks together with active transistor electronics, allowing substantial size reduction. In essence, MEMS technology may eventually allow replacement of off-chip SAW and crystal technologies by on-chip vibrating micromechanical resonators with comparable *Q* and performance. Indeed, reductions in size and board-level packaging complexity, as well as the desire for the high performance attainable by super-heterodyne architectures, are principal drivers for this technology.

Although size reduction is certainly an advantage of this technology (commonly dubbed "RF MEMS"), it merely touches upon a much greater potential to influence general methods for signal processing. In particular, since they can now be integrated (perhaps on a massive scale) using MEMS technology, vibrating ∝mechanical resonators (or ∝mechanical links) can now be thought of as tiny circuit elements, much like resistors or transistors, in a new mechanical circuit technology. Like a single transistor, a single mechanical link does not possess adequate processing power for most applications. However, again like transistors, when combined into larger (potentially, VLSI) circuits, the true power of ∝mechanical links can be unleashed, and signal processing functions with attributes previously inaccessible to transistor circuits may become feasible. This in turn can lead to architectural changes for communication transceivers. MEMS technology may in fact make its most important impact not at the component level, but at the system level, by offering alternative transceiver architectures that emphasize selectivity to substantially reduce power consumption and enhance performance.

This chapter focuses upon communication sub-system performance enhancements potentially attainable via use of vibrating micromechanical resonator circuits in MEMS-based transceiver architectures. Section 2 begins by reviewing the issues involved with transceiver miniaturization, specifically focusing on the need for high-*Q*. Section 3 follows with an overview of various micromechanical signal processing circuits, describing micromechanical tanks, filters, mixer-filters, and switches, and providing sufficient detail to facilitate the incorporation of such circuits into communication sub-sys-

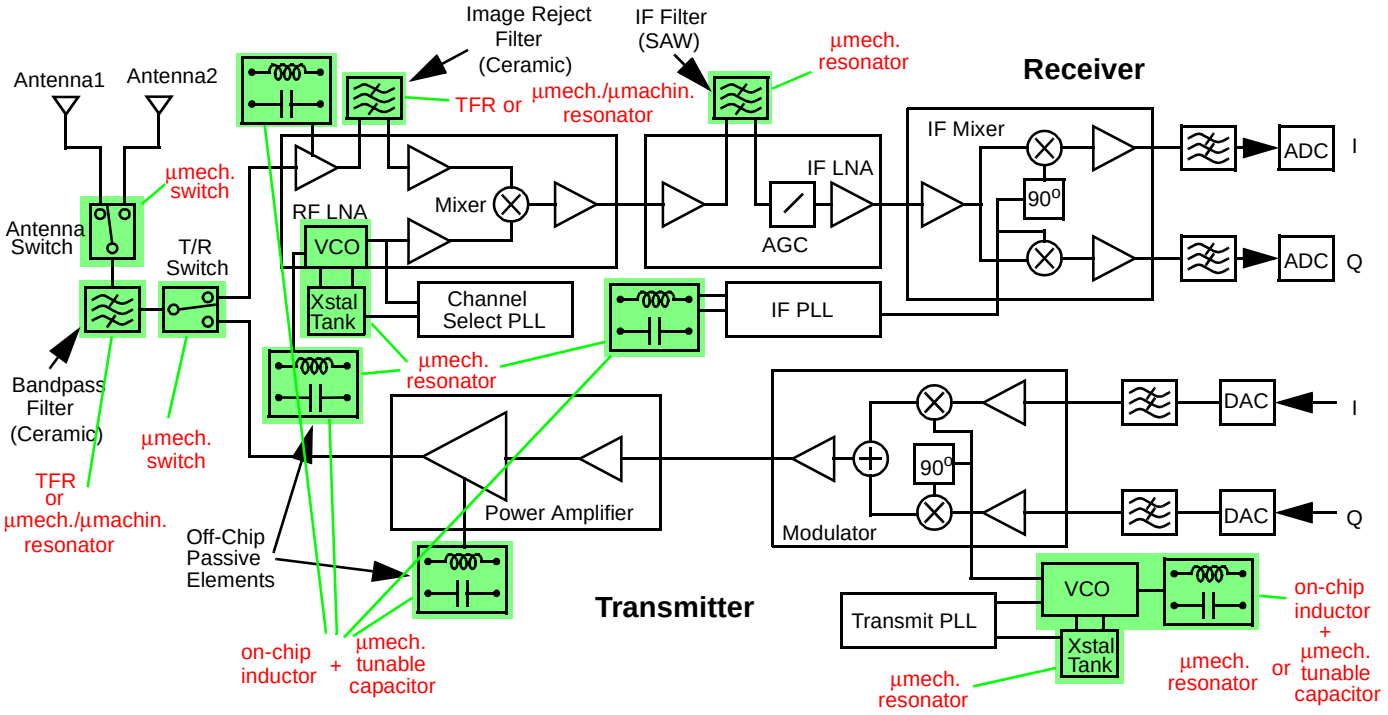

Fig. 1: System-level schematic detailing the front-end design for a typical wireless transceiver. The off-chip, high-*Q*, passive components targeted for replacement via micromechanical versions (suggestions in lighter ink) are indicated in the figure.

tems. Specific transceiver architectures using such devices are then presented in Sections 4 and 5, with a focus on the specific performance enhancements afforded by each approach. Section 6 then serves as a reminder that this is still a fledgling technology, emphasizing the present limitations of this technology and giving a sprinkling of the specific research problems that must be solved before the architectures of Sections 4 and 5 can become a reality. Sections 7 and 7.4.1 finally close the chapter with details on techniques for combining mechanical and transistor circuits onto single chips.

2. Miniaturization of Transceivers

To illustrate more concretely the specific transceiver functions that can benefit from micromechanical implementations (to be discussed), Fig. 1 presents the system-level schematic for a typical super-heterodyne wireless transceiver. As implied in the figure, several of the constituent components can already be miniaturized using integrated circuit transistor technologies. These include the low noise amplifiers (LNA's) in the receive path, the solid-state power amplifier (SSPA) in the transmit path, synthesizer phase-locked loop (PLL) electronics, mixers, and lower frequency digital circuits for baseband signal demodulation. Due to noise, power, and frequency considerations, the SSPA (and sometimes the LNA's) are often implemented using compound semiconductor technologies (i.e., GaAs). Thus, they often occupy their own chips, separate from the other mentioned transistor-based components, which are normally realized using silicon-based bipolar and CMOS technologies. However, given the rate of improvement of silicon technologies (silicon-germanium included [14]), it is not implausible that all of the above functions could be integrated onto a single-chip in the foreseeable future.

Unfortunately, placing all of the above functions onto a single chip does very little towards decreasing the overall super-heterodyne transceiver size, which is dominated not by transistor-based components, but by the numerous passive components indicated in Fig. 1. The presence of so many frequency-selective passive components is easily justified when considering that communication systems designed to service large numbers of users require numerous communication channels, which in many implementations (e.g., Time Division Multiple Access (TDMA)) must have small bandwidths and must be separable by transceiver devices used by the system. The requirement for small channel bandwidths results in a requirement for extremely selective filtering devices for channel selection and extremely stable (noise free) local oscillators for frequency translation. For the vast majority of cellular and cordless standards, the required selectivity and stability can only be achieved using high-*Q* components, such as discrete inductors, discrete tunable capacitors (i.e., varactors), and SAW and quartz crystal resonators, all of which interface with IC components at the board level. The needed performance cannot be achieved using conventional IC technologies, because such technologies lack the required *Q*. It is for this reason that virtually all commercially available cellular or cordless phones contain numerous passive SAW and crystal components.

2.1. The Need for High *Q* in Oscillators

For any communications application, the stability of the oscillator signals used for frequency translation, synchronization, or sampling, is of utmost importance. Oscillator frequencies must be stable against variations in temperature, against

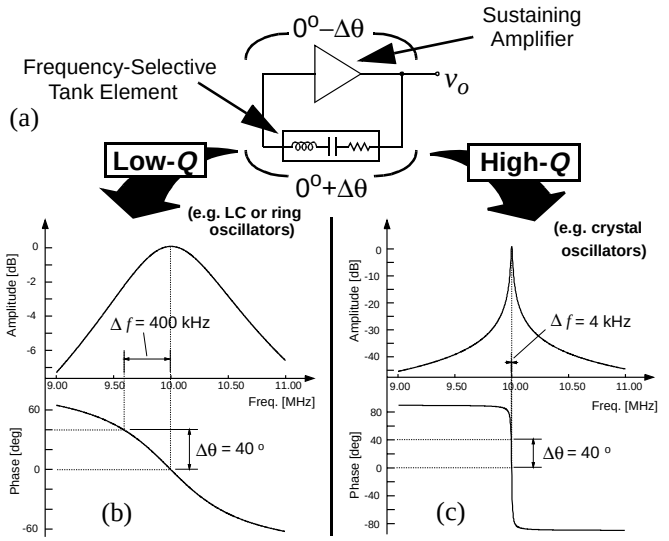

Fig. 2: (a) A simple series resonant oscillator schematic (b) Bode plot for a low Q tank, indicating the Δf for a given $\Delta\theta$. (c) Similar to (b), but for a high Q tank.

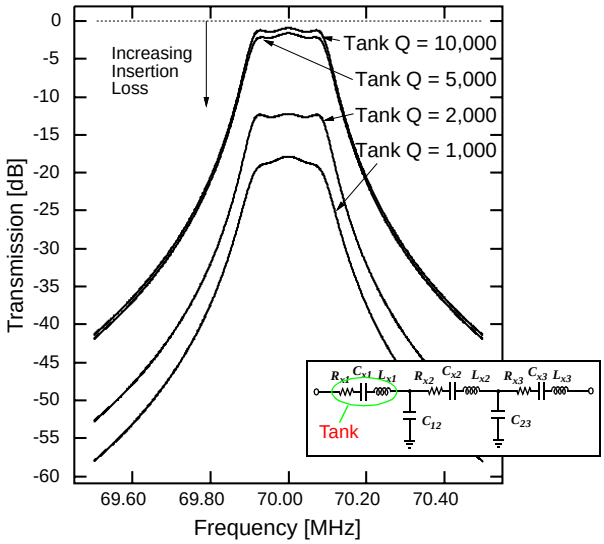

Fig. 3: Simulated frequency characteristics for a 0.3% bandwidth, 70 MHz bandpass filter under varying tank Q's.

aging, and against any phenomena, such as noise or microphonics, that cause instantaneous fluctuations in phase and frequency. The single most important parameter that dictates oscillator stability is the Q of the frequency-setting tank (or of the effective tank for the case of ring oscillators). For a given application, and assuming a finite power budget, adequate long- and short-term stability of the oscillation frequency is insured only when the tank Q exceeds a certain threshold value.

The correlation between tank Q and oscillator stability can be illustrated heuristically by considering the simple oscillator circuit depicted in Fig. 2(a). Here, a series resonant oscillator is shown, comprised of a sustaining amplifier and an LC tank connected in a positive feedback loop. For proper start-up and steady-state operation, the total phase shift around the loop must sum to zero. Thus, if at the oscillation frequency the amplifier operates nominally with a 0^o phase shift from its input to its output, then the tank must also have a 0^o phase shift across its terminals. Given this, and referring to any one of the tank response spectra shown in Figs. 2(b) or (c), this oscillator is seen to operate nominally at the tank resonance frequency. If, however, an external stimulus (e.g., a noise spike, or a temperature fluctuation) generates a phase shift $-\Delta\theta$ across the terminals of the sustaining amplifier, the tank must respond with an equal and opposite phase shift $\Delta\theta$ for sustained oscillation. As dictated by the tank transfer functions of Fig. 2, any tank phase shift must be accompanied by a corresponding operating frequency shift Δf. The magnitude of Δf for a given $\Delta\theta$ is largely dependent on the Q of the resonator tank. Comparison of Fig. 2(b) with (c) clearly shows that a given phase shift incurs a much smaller frequency deviation on the tank with the higher Q. Thus, the higher the tank Q, the more stable the oscillator against phase-shifting phenomena.

To help quantify the above heuristic concepts, one important figure of merit for oscillators is the phase noise power present at frequencies close to the carrier frequency. Typical phase noise requirements range from –128 dBc/Hz at 600 kHz deviation from a 915-980 MHz carrier in European Global System for Mobile Telecommunications (GSM) cellular phones, to –150 dBc/Hz at 67 kHz carrier deviations in X-Band, Doppler-based radar systems [15]. Through a more rigorous analysis of Fig. 2 (assuming linear operation), the $1/f^2$ phase noise of a given oscillator can be described by the expression [16]:

$$\left(\frac{N_{op}}{C}\right)_{f_m} = \frac{FkT}{C}\frac{1}{8Q^2}\left(\frac{f_o}{f_m}\right)^2 \quad [\text{dBc/Hz}]\,, \qquad (1)$$

where $(N_{op}/C)_{fm}$ is the phase noise power density-to-carrier power ratio at a frequency f_m offset from the carrier frequency, F is the noise figure of the active device evaluated using the total oscillator power P, C is the carrier power delivered to the load, and f_o is the carrier frequency. From (1), phase noise is seen to be inversely proportional to the square of Q, and directly proportional to the amplifier noise figure F. Given that F can often be reduced by increasing the operating power P of the sustaining amplifier, and that C increases or decreases with P, (1) then can be interpreted as implying that power and Q can be traded to achieve a given phase noise specification. Given the need for low power in portable units, and given that the synthesizer (containing the reference and VCO oscillators) is often a dominant contributor to total transceiver power consumption, modern transceivers could benefit greatly from technologies that yield high-Q tank components.

2.2. The Need for High Q in Filters

Tank Q also greatly influences the ability to implement extremely selective IF and RF filters with small percent bandwidth, small shape factor, and low insertion loss. To illustrate, Fig. 3 presents simulated frequency characteristics under varying resonator tank Q's for a 0.3% bandwidth bandpass filter centered at 70 MHz, realized using the typical LC resonator ladder configuration shown in the insert. As shown, for a resonator tank Q of 10,000, very little insertion loss is observed. However, as tank Q decreases, insertion loss increases very

quickly, to the point where a tank Q of 1,000 leads to 20 dB of insertion loss—too much even for IF filters, and quite unacceptable for RF filters. As with oscillators, high-Q tanks are required for RF and IF filters alike, although more so for the latter, since channel selection is done predominantly at the IF in super-heterodyne receivers. In general, the more selective the filter, the higher the resonator Q required to achieve a given level of insertion loss. In particular, the above 0.3% bandwidth filter example applies for IF filters, which, because of their high selectivity, are best implemented with resonator Q's exceeding 5,000; RF pre-select or image-reject filters, on the other hand, typically require only 3% bandwidths and can thus be implemented using resonators with Q's on the order of 500-1,000.

3. Micromechanical Circuits

Although mechanical circuits, such as quartz crystal resonators and SAW filters, provide essential functions in the majority of transceiver designs, their numbers are generally suppressed due to their large size and finite cost. Unfortunately, when minimizing the use of high-Q components, designers often trade power for selectivity (i.e., Q), and hence, sacrifice transceiver performance. As a simple illustration, if the high-Q IF filter in the receive path of a communication subsystem is removed, the dynamic range requirement on the subsequent IF amplifier, IQ mixer, and A/D converter circuits, increases dramatically, forcing a corresponding increase in power consumption. Similar trade-offs exist at RF, where the larger the number or greater the complexity of high-Q components used, the smaller the power consumption in surrounding transistor circuits.

By shrinking dimensions and introducing batch fabrication techniques, MEMS technology provides a means for relaxing the present constraints on the number and complexity of mechanical circuits, perhaps with implications not unlike those that integrated circuit technology had on transistor circuit complexity. Before exploring the implications, specific μmechanical circuits are first reviewed, starting with the basic building block elements used for mechanical circuits, then expanding with descriptions of the some of most useful linear and nonlinear mechanical circuits.

3.1. The Micromechanical Beam Element

To date, the majority of μmechanical circuits most useful for communication applications in the VHF range have been realized using μmechanical flexural-mode beam elements, such as shown in Fig. 4 with clamped-clamped boundary conditions [11], [12], [18]. Although several micromachining technologies are available to realize such an element in a variety of different materials, surface micromachining has been the preferred method for μmechanical communication circuits, mainly due to its flexibility in providing a variety of beam end conditions and electrode locations, and its ability to realize very complex geometries with multiple levels of suspension.

Figure 5 summarizes the essential elements of a typical surface-micromachining process tailored to produce a clamped-clamped beam. In this process, a series of film depositions and

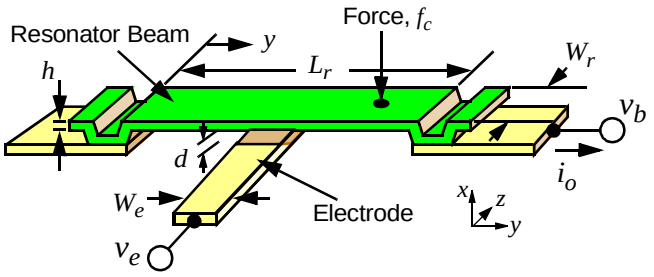

Fig. 4: Perspective-view schematic of a clamped-clamped beam μmechanical resonator in a general bias and excitation configuration.

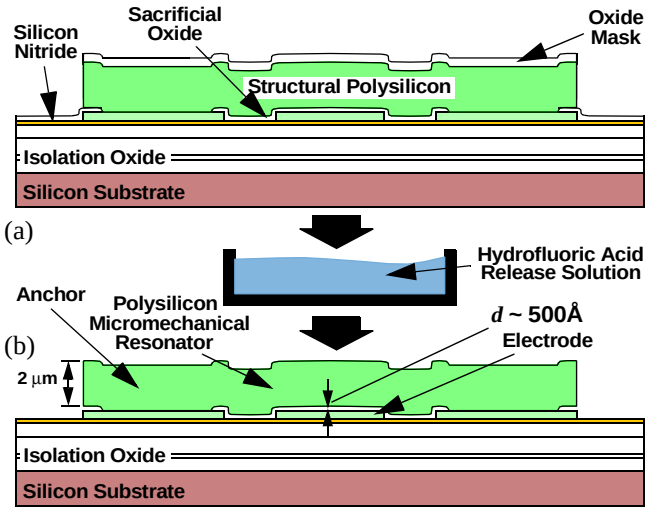

Fig. 5: Cross-sections describing surface micromachining. (a) Required film layers up to the release etch step. (b) Resulting free-standing beam following a release etch in hydrofluoric acid.

lithographic patterning steps—identical to similar steps used in planar IC fabrication technologies—are utilized to first achieve the cross-section shown in Fig. 5(a). Here, a sacrificial oxide layer supports the structural polysilicon material during deposition, patterning, and subsequent annealing. In the final step of the process, the wafer containing cross-sections similar to Fig. 5(a) is dipped into a solution of hydrofluoric acid, which etches away the sacrificial oxide layer without significantly attacking the polysilicon structural material. This leaves the free-standing structure shown in Fig. 5(b), capable of movement in three dimensions, if necessary, and more importantly, capable of vibrating with high Q and good temperature stability, with temperature coefficients on the order of –10 ppm/^{o}C [17]. Figure 6 presents the scanning electron micrograph (SEM) of a clamped-clamped beam polysilicon micromechanical resonator designed to operate at 17.4 MHz.

For communications applications, clamped-clamped [18] and free-free [11] flexural-mode beams with Q's on the order of 10,000 (in vacuum) and temperature coefficients on the order of –12ppm/^{o}C, have been popular for the VHF range, while thin-film bulk acoustic resonators [19]-[21] (Q~1,000) have so far addressed the UHF range. To simplify the discussion, and because they have so far been the most amenable to the implementation of mechanical circuits, the remainder of this section focuses on clamped-clamped beam μmechanical resonators.

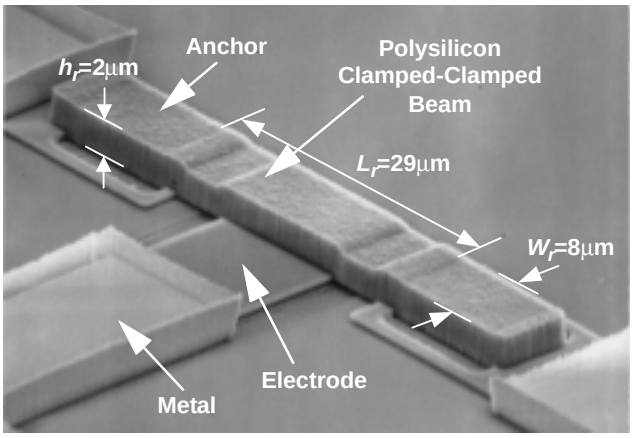

Fig. 6: SEM of a 17.4 MHz polysilicon clamped-clamped beam micromechanical resonator with metallized electrodes.

3.2. Clamped-Clamped Beam Micromechanical Resonators

As previously mentioned, Fig. 4 presents the perspective-view schematic for a clamped-clamped beam μmechanical resonator, indicating key dimensions and showing a general bias and excitation configuration. As shown, this device consists of a beam anchored (i.e., clamped) at both ends, with an electrode underlying its central locations. Both the beam and electrode are constructed of conductive materials, with doped polycrystalline silicon being the most common to date. Note that both electrical and mechanical inputs are possible for this device.

For frequency reference, filtering, and mixing applications, the vibrational resonance frequency f_o of this flexural-mode mechanical beam is of great interest. The fundamental resonance frequency of the clamped-clamped beam of Fig. 4 is given by the expression [18]

$$f_o = \frac{1}{2\pi}\sqrt{\frac{k_r}{m_r}} = 1.03\kappa\sqrt{\frac{E}{\rho}}\frac{h}{L_r^2}(1-g(V_P))^{1/2}, \qquad (2)$$

where E and ρ are the Young's modulus and density of the structural material, respectively; h and L_r are specified in Fig. 4; the function g models the effect of an electrical spring stiffness k_e that appears when electrodes and voltages are introduced and that subtracts from the mechanical stiffness k_m; and κ is a scaling factor that models the effects of surface topography in actual implementations [18]. From (2), geometry clearly plays a major role in setting the resonance frequency, and in practice, attaining a specified frequency amounts to CAD layout of the proper dimensions. Table 1 presents expected resonance frequencies for various beam dimensions, modes, and structural materials, showing a wide range of attainable frequencies, from VHF to UHF.

3.2.1. Electrical Excitation

As shown in Fig. 4, this device accepts two electrical inputs, v_e and v_b, applied to the electrode and beam, respectively. In this configuration, the difference voltage $(v_e - v_b)$ is effectively applied across the electrode-to-resonator capacitor gap, generating a force between the stationary electrode and movable beam given by

Table 1: μMechanical Resonator Frequency Design*

Freq. [MHz]	Material	Mode	h_r [μm]	W_r [μm]	L_r [μm]
70	silicon	1	2	8	15.18
110	silicon	1	2	8	11.86
250	silicon	1	2	4	7.34
870	silicon	2	4	4	7.13
870	diamond	1	4	4	6.47
1800	silicon	2	4	8	4.98
1800	diamond	2	4	4	7.58

* Determined for free-free beams using Timoshenko methods that include the effects of finite h and W_r [11].

$$F_d = -\frac{\partial E}{\partial x} = -\frac{1}{2}(v_e - v_b)^2\frac{\partial C}{\partial x} = -\frac{1}{2}(v_b^2 - 2v_b v_e + v_e^2)\frac{\partial C}{\partial x} \qquad (3)$$

where x is displacement (with direction indicated in Fig. 4), and $(\partial C/\partial x)$ is the change in resonator-to-electrode capacitance per unit displacement, approximately given by (neglecting fringing fields and static beam bending)

$$\frac{\partial C}{\partial x} = \frac{\varepsilon_o W_r W_e}{d_o^2}, \qquad (4)$$

where d_o is the electrode-to-resonator gap spacing under static (non-resonance) conditions, and ε_o is the permittivity in vacuum. When using the resonator as a tank or filter circuit (as opposed to a mixer, to be discussed later), a dc-bias voltage V_P is applied to the conductive beam, while an ac excitation signal $v_i = V_i\cos\omega_i t$ is applied to the underlying electrode. In this configuration, (3) reduces to

$$F_d = -\frac{\partial C}{\partial x}\left(\frac{V_P^2}{2} + \frac{V_i^2}{4}\right) + V_P\frac{\partial C}{\partial x}V_i\cos\omega_i t - \frac{\partial C}{\partial x}\frac{V_i}{4}\cos 2\omega_i t \qquad (5)$$

The first term in (5) represents an off-resonance dc force that statically bends the beam, but that otherwise has little effect on its signal processing function, especially for VHF and above frequencies, for which the beam stiffness is very large. The second term constitutes a force at the frequency of the input signal, amplified by the dc-bias voltage V_P, and is the main input component used in high-Q tank and filter applications. When $\omega_i = \omega_o$ (the radian resonance frequency) this force drives the beam into resonance, with a zero-to-peak displacement amplitude at location y given by

$$x(y) = \frac{QF_d}{k_{reff}(y)} = \frac{Q}{k_{reff}(y)}V_P\frac{\partial C}{\partial x}v_i, \qquad (6)$$

where $k_{reff}(y)$ is an effective stiffness at location y to be determined later in this section via integration over the electrode width. Motion of the beam creates a dc-biased (via V_P) time-varying capacitance between the electrode and resonator that sources an output current given by

$$i_o = V_P\frac{\partial C}{\partial x}\frac{\partial x}{\partial t} \qquad (7)$$

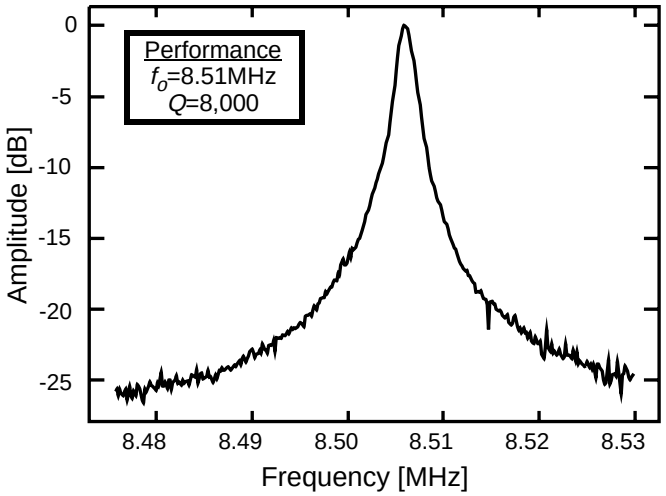

Fig. 7: Frequency characteristic for an 8.5 MHz polysilicon μmechanical resonator measured under 70mTorr vacuum using a dc-bias voltage V_P=10V, a drive voltage of v_i=3mV, and a transresistance amplifier with a gain of 33kΩ to yield an output voltage v_o. Amplitude = v_o/v_i. [18]

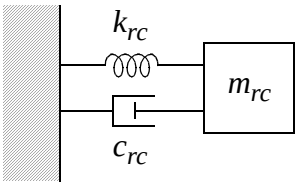

Fig. 8: Lumped-parameter mechanical equivalent circuit for the micromechanical resonator of Fig. 4.

When plotted versus the frequency of v_i, i_o traces out a bandpass biquad characteristic with a Q ~10,000 (c.f., Fig. 7 [18])—very suitable for reference oscillators and low-insertion loss filters. Note, however, that this Q is only achievable under vacuum, where viscous gas damping is minimized [22]. Much lower Q's on the order of hundreds are seen under atmospheric pressure.

The third term in (5) represents a term capable of driving the beam into vibration when $\omega_i=(1/2)\omega_o$. If V_P is very large compared with V_i, this term is greatly suppressed, but it can be troublesome for bandpass filters in cases where very large interferers are present at half the passband frequency. In these cases, a μmechanical notch filter at $(1/2)\omega_o$ may be needed.

3.2.2. Equivalent Lumped Parameter Mechanical Circuit

For the purposes of mechanical circuit design, it is often convenient to define an equivalent lumped-parameter mass-spring-damper mechanical circuit for this resonator (c.f., Fig. 8), with element values that vary with location on the resonator. With reference to Fig. 9, the equivalent mass at a location y on the resonator is given by [23]

$$m_r(y) = \frac{KE_{tot}}{(1/2)(v(y))^2} = \frac{\rho W_r h \int_0^{L_r} [X_{mode}(y')]^2 dy'}{[X_{mode}(y)]^2} \qquad (8)$$

where

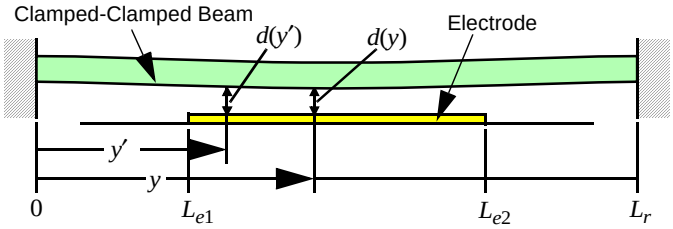

Fig. 9: Resonator cross-sectional schematic for frequency-pulling and impedance analysis.

$$X_{mode}(y) = \zeta(\cos\beta y - \cosh\beta y) + (\sin\beta y - \sinh\beta y), \qquad (9)$$

β=4.730/L_r and ζ=–1.01781 for the fundamental mode, KE_{tot} is the peak kinetic energy in the system, $v(y)$ is the velocity at location y, and dimensional parameters are given in Fig. 9. The equivalent spring stiffness follows readily from (2) and (8), and is given by

$$k_r(y) = \omega_o^2 m_r(y), \qquad (10)$$

where ω_o is the radian resonance frequency of the beam. Finally, the damping factor is given by

$$c_r(y) = \frac{\sqrt{k_m(y)m_r(y)}}{Q_{nom}} = \frac{\omega_{nom}m_r(y)}{Q_{nom}} = \frac{k_m(y)}{\omega_{nom}Q_{nom}}, \qquad (11)$$

where

$$k_m(y) = \omega_{nom}^2 m_r(y) \qquad (12)$$

is the mechanical stiffness of the resonator alone, without the influence of applied voltages and electrodes to be discussed next, and Q_{nom} is the quality factor of the resonator under the same conditions.

3.2.3. Voltage-Tunable Electrical Stiffness

As indicated in (2), where g is seen to be a function of dc-bias voltage V_P, the resonance frequency of this device is tunable via adjustment of V_P [24], [25] and this can be used advantageously to implement filters with tunable center frequencies, or to correct for passband distortion caused by finite planar fabrication tolerances. The dc-bias dependence of resonance frequency arises from a V_P-dependent electrical spring constant k_e that subtracts from the mechanical spring constant of the system k_m, lowering the overall spring stiffness $k_r=k_m-k_e$, thus, lowering the resonance frequency according to the expression

$$\begin{aligned} f_o &= \frac{1}{2\pi}\sqrt{\frac{k_m - k_e}{m_r}} = \frac{1}{2\pi}\sqrt{\frac{k_m}{m_r}}\left[1 - \left\langle\frac{k_e}{k_m}\right\rangle\right]^{1/2} \\ &= 1.03\kappa\sqrt{\frac{E}{\rho}}\frac{h}{L^2}\left[1 - \left\langle\frac{k_e}{k_m}\right\rangle\right]^{1/2} \end{aligned} \qquad (13)$$

where k_m and m_r denote values at a particular location (usually the beam center location), and the quantity $\langle k_e/k_m\rangle$ must be obtained via integration over the electrode width W_e due to the location dependence of k_m.

The electrical spring stiffness k_e is generated by the nonlinear dependence of electrode-to-resonator gap capacitance $C(x)$ on displacement x, and is dependent very strongly upon the

electrode-to-resonator gap spacing d. At a specific location y' centered on an infinitesimally small width of the electrode dy', the differential in electrical stiffness is given by [25]

$$dk_e(y') = V_P^2 \frac{\varepsilon_o W_r dy'}{(d(y'))^3}, \quad (14)$$

where the electrode-to-resonator gap distance d is now seen to also be location dependent, since the beam bends somewhat due to the dc-bias V_P applied between the electrode and resonator. Recognizing that for the fundamental mode the static and dynamic stiffnesses are virtually the same, and assuming a static bending shape due to the distributed dc force defined by the function $X_{static}(y)$, the gap distance can be expressed as

$$d(y) = d_o - \frac{1}{2} V_P^2 \varepsilon_o W_r \int_{L_{e1}}^{L_{e2}} \frac{1}{k_m(y')(d(y'))^2} \frac{X_{static}(y)}{X_{static}(y')} dy', \quad (15)$$

where d_o is the static electrode-to-resonator gap with V_P=0V. In (15), the second term represents the static displacement of the resonator towards the electrode at a particular location y, evaluated by integration over the width of the electrode, from y=L_{e1} to L_{e2}. For the common case where the electrode is centered with the resonator beam center, L_{e1}=0.5(L_r−W_e) and L_{e2}=0.5(L_r+W_e). Since the desired variable $d(y)$ appears on both sides of (15), one of them within an integral, (15) is best solved by first assuming $d(y)$=d_o on the right side, solving for $d(y)$ on the left, then using this function again on the right, iterating until $d(y)$ converges. In addition, for most cases (15) is not overly sensitive to the function $X_{static}(y)$, so $X_{mode}(y)$ given by (9) can be substituted for $X_{static}(y)$ with little difference.

The quantity $\langle k_e/k_m \rangle$ may now be found by integrating over the electrode width, and is given by

$$\left\langle \frac{k_e}{k_m} \right\rangle = g(d, V_P) = \int_{L_{e1}}^{L_{e2}} \frac{dk_e(y')}{k_m(y')}. \quad (16)$$

3.2.4. Pull-In Voltage, V_{PI}

When the applied dc-bias voltage V_P is sufficiently large, catastrophic failure of the device ensues, in which the resonator beam is pulled down onto the electrode. This leads to either destruction of the device due to excessive current passing through the now shorted electrode-to-resonator path, or at least a removal of functionality if a dielectric layer (e.g., an oxide or nitride) is present above the electrode to prevent electrical contact between it and the conductive resonator beam.

Unlike low-frequency micromechanical structures, such as used in accelerometers or gyroscopes [26], [27], the attractive electrostatic force between the electrode and this high-frequency resonator that incites pull-down now acts against a very large distributed stiffness that must be integrated over the electrode area to accurately predict the pull-down voltage V_{PI}. Thus, previously used closed-form expressions for V_{PI} [25] based on lumped parameter analysis are no longer applicable. Rather, for resonators with the design of Fig. 4 and beam lengths less than 50 μm, the procedure for determining V_{PI} entails finding the V_P that sets the resonance frequency equal to zero. With reference to (13), this amounts to setting (16) equal to unity and solving for the V_P variable.

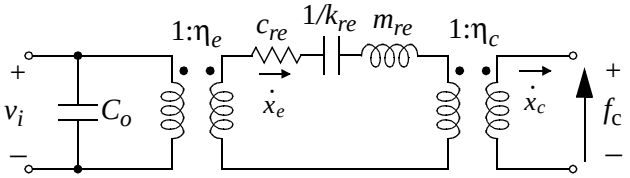

Fig. 10: Equivalent circuit for a μmechanical resonator with both electrical (voltage v_i) and mechanical (force f_c) inputs and outputs.

Table 2: Mechanical-to-Electrical Correspondence in the Current Analogy

Mechanical Variable	Electrical Variable
Damping, c	Resistance, R
Stiffness^{-1}, k^{-1}	Capacitance, C
Mass, m	Inductance, L
Force, f	Voltage, V
Velocity, v	Current, I

3.2.5. Small-Signal Electrical Equivalent Circuit

To conveniently model and simulate the impedance behavior of this μmechanical resonator in an electromechanical circuit, an electrical equivalent circuit is needed. As shown in Fig. 4, both electrical and mechanical inputs and outputs are possible for this device, so the equivalent circuit must be able to model both. In addition, for physical consistency from both transducer and noise perspectives, a circuit model that directly uses the lumped mechanical elements summarized by (8)-(11) is preferred. Figure 10 presents one of the more useful equivalent circuits used for linear mechanical circuit design [18], [28], in which transformers model both electrical and mechanical couplings to and from the resonator, which itself is modeled by a core *LCR* circuit—the electrical analogy to a mass-spring-damper system—with element values corresponding to actual values of mass, stiffness, and damping as given by (8)-(11). In this circuit, the current electromechanical analogy is utilized, summarized in Table 2.

When looking into the electrode port of the equivalent resonator circuit of Fig. 10, a transformed *LCR* circuit is seen, with element values given by

$$L_x = \frac{m_{re}}{\eta_e^2} \qquad C_x = \frac{\eta_e^2}{k_{re}} \qquad R_x = \frac{\sqrt{k_{re} m_{re}}}{Q \eta_e^2} = \frac{c_{re}}{\eta_e^2}, \quad (17)$$

where the subscript e denotes the electrode location at the very center of the resonator beam (i.e., at y=L_r/2). An expression for the electromechanical transformer turns ratio η_e can be obtained via an impedance analysis yielding the motional resistance R_x seen across the electrode-to-resonator gap at resonance. Pursuant to this, the voltage-to-displacement transfer function at a given location y (c.f., Fig. 9) at resonance is first found using phasor forms of (4), (5), (6), (9), and (10), and integrating over the electrode width to yield

$$\frac{X}{V_i}(y) = \int_{L_{e1}}^{L_{e2}} \frac{Q V_P \varepsilon_o W_r}{[d(y')]^2 k_r(y')} \frac{X_{mode}(y)}{X_{mode}(y')} dy'. \quad (18)$$

Using the phasor form of (7), the series motional resistance seen looking into the drive electrode is then found to be

$$R_x = \frac{V_i}{I_x} = \left[\int_{L_{e1}}^{L_{e2}} \frac{\omega_o V_P \varepsilon_o W_r}{[d(y)]^2} \cdot \frac{X}{V_i}(y)dy\right]^{-1} \quad (19)$$

Inserting (18), factoring out $c_{re}=k_{re}/(\omega_o Q)$, and extracting η_e yields

$$\eta_e = \sqrt{\int_{L_{e1}}^{L_{e2}}\int_{L_{e1}}^{L_{e2}} \frac{V_P^2(\varepsilon_o W_r)^2}{[d(y')d(y)]^2}\frac{k_{re}}{k_r(y')}\frac{X_{mode}(y)}{X_{mode}(y')}dy'dy}\,. \quad (20)$$

Note that the effective integrated stiffness defined in (6) can also be extracted from (18), yielding

$$k_{reff}(y) = \left[\int_{L_{e1}}^{L_{e2}}\left[\frac{d_o}{d(y')}\right]^2 \frac{1}{k_r(y')}\frac{1}{W_e}\frac{X_{mode}(y)}{X_{mode}(y')}dy'\right]^{-1} \quad (21)$$

The transformer turns ratio η_c in Fig. 10 models the mechanical impedance transformation achieved by mechanically coupling to the resonator at a *y* location displaced from its center. As will be seen, such coupling is required when implementing filters with two or more resonators. Expressed in terms of a stiffness ratio, the equation for the mechanical transformer turns ratio when coupling at a distance l_c from an anchor takes the form

$$\eta_c = \sqrt{\frac{k_r(l_c)}{k_{re}}}\,. \quad (22)$$

Finally, for the equivalent circuit of Fig. 10, it should be noted that the damping constant c_r is not inherently a function of the electrical stiffness k_e. Thus, when expressed in terms of the overall stiffness k_r of the system, the *Q* of the resonator must be adjusted so that c_r retains its original value given by (11). In terms of k_r and ω_o, then, expressions for c_r take on the form

$$c_r = \frac{\omega_o m_r}{Q} = \frac{k_r}{\omega_o Q} = \frac{\sqrt{k_r m_r}}{Q}, \quad (23)$$

where

$$Q = Q_{nom}\left[1 - \langle\frac{k_e}{k_m}\rangle\right]^{1/2}. \quad (24)$$

Note that the effective resonator quality factor *Q* is dependent upon the electrical spring stiffness k_e, and thus, is also a function of the dc-bias voltage V_P. In this chapter, the variable *Q* denotes that defined by (24), while Q_{nom} is reserved for zero-bias conditions.

In the design of μmechanical circuits comprised of interlinked beams, the equivalent circuit in Fig. 10 functions in a similar fashion to the hybrid-π small-signal equivalent circuit used for analog transistor circuit design. The main difference between mechanical links and transistors are the basic features that make them useful as circuit elements: while transistors exhibit high gain, mechanical links exhibit very large *Q*. By combining the strong points of both circuit elements, on-chip functions previously unachievable are now within the realm of possibilities. We now touch upon a few of these.

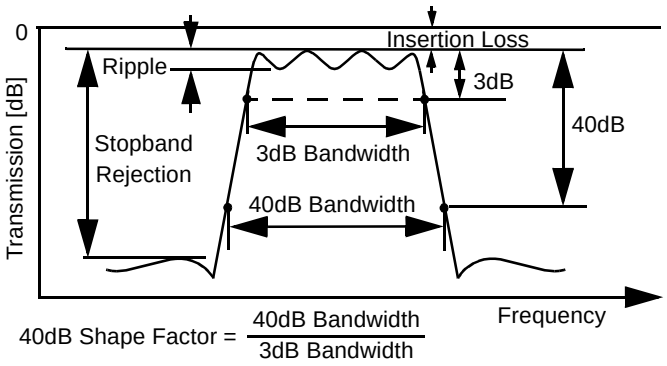

Fig. 11. Parameters typically used for filter specification.

3.3. Micromechanical Filters

Among the more useful μmechanical circuits for communications are those implementing low-loss bandpass filters, capable of achieving frequency characteristics as shown in Fig. 11, where a broader frequency passband than achievable by a single resonator beam is shown, with a sharper roll-off to the stopband (i.e., smaller shape factor).

To achieve the characteristic of Fig. 11, a number of micromechanical resonators are coupled together by soft coupling springs [18], [23], [29], [30], as illustrated schematically in Fig. 12(a) using ideal mass-spring-damper elements. By linking resonators together using (ideally) massless springs, a coupled resonator system is achieved that now exhibits several modes of vibration. As illustrated in Fig. 13 for the coupled three-resonator system of Fig. 12, the frequency of each vibration mode corresponds to a distinct peak in the force-to-displacement frequency characteristic, and to a distinct, physical mode shape of the coupled mechanical resonator system. In the lowest frequency mode, all resonators vibrate in phase; in the middle frequency mode, the center resonator ideally remains motionless, while the end resonators vibrate 180^o out of phase; and finally, in the highest frequency mode, each resonator is phase-shifted 180^o from its adjacent neighbor. Without additional electronics, the complete mechanical filter exhibits the jagged passband seen in Fig. 13. As will be shown, termination resistors designed to lower the *Q*'s of the input and output resonators by specific amounts are required to flatten the passband and achieve a more recognizable filter characteristic, such as in Fig. 11.

In practical implementations, because planar IC processes typically exhibit substantially better *matching* tolerances than *absolute*, the constituent resonators in μmechanical filters are normally designed to be identical, with identical dimensions and resonance frequencies. For such designs, the center frequency of the overall filter is equal to the resonance frequency f_o of the resonators, while the filter passband (i.e., the bandwidth) is determined by the spacings between the mode peaks.

The relative placement of the vibration peaks in the frequency characteristic—and thus, the passband of the eventual filter—is determined primarily by the stiffnesses of the coupling springs (k_{sij}) and of the constituent resonators at the cou-

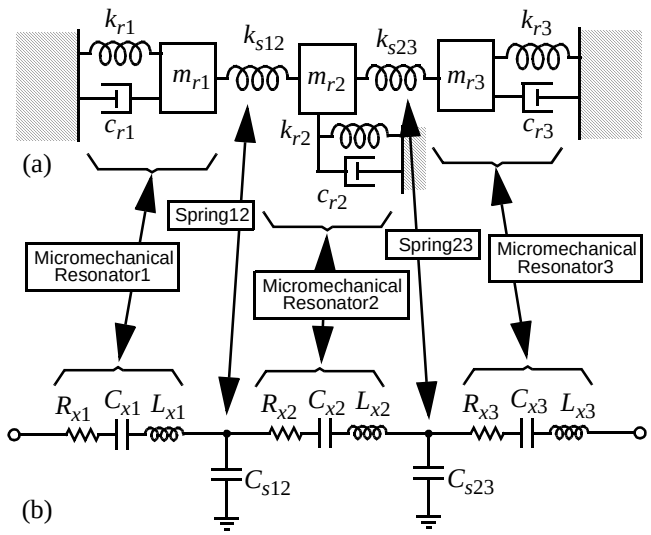

Fig. 12. (a) Equivalent lumped parameter mechanical circuit for a mechanical filter. (b) Corresponding equivalent *LCR* network.

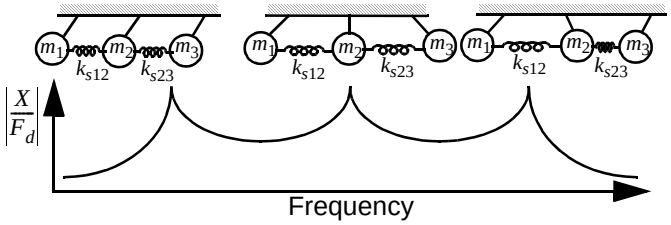

Fig. 13. Mode shapes of a three-resonator micromechanical filter and their corresponding frequency peaks.

pling locations (k_r). Specifically, for a filter with center frequency f_o and bandwidth B, these stiffnesses must satisfy the expression [23]

$$B = \left(\frac{f_o}{k_{ij}}\right)\left(\frac{k_{sij}}{k_r}\right) \tag{25}$$

where k_{ij} is a normalized coupling coefficient found in filter cookbooks [31]. Note from (25) that filter bandwidth is not dependent on the absolute values of resonator and coupling beam stiffness; rather, their ratio k_{sij}/k_r dictates bandwidth. Thus, the procedure for designing a mechanical filter involves two main steps (not necessarily in this order): first, design of a mechanical resonator with resonance frequency f_o and adjustable stiffness k_r; and second, design of coupling springs with appropriate values of stiffness k_{sij} to enable a desired bandwidth within the adjustment range of resonator k_r's.

To take advantage of the maturity of *LC* ladder filter synthesis techniques, the enormous database governing *LC* ladder filter implementations [31], and the wide availability of electrical circuit simulators, realization of the μmechanical filter of Fig. 12(a) often also involves the design of an *LC* ladder version to fit the desired specification. The elements in the *LC* ladder design are then matched to lumped mechanical equivalents via electromechanical analogy, where inductance, capacitance, and resistance in the electrical domain equate to mass, compliance, and damping, respectively, in the mechanical domain. Figure 12(b) explicitly depicts the equivalence between the filter's lumped mass-spring-damper circuit and its electrical equivalent circuit. As shown, for this particular electromechanical analogy (the current analogy), each constituent resonator corresponds to a series *LCR* tank, while each (massless) coupling spring ideally corresponds to a shunt capacitor, with the whole coupled network corresponding to an *LC* ladder bandpass filter. It should be emphasized that the circuit in Fig. 12(b) corresponds to the ideal mechanical circuit of Fig. 12(a), in which the resonators are modeled by simple lumped elements, and coupling springs are considered massless. As will be seen, additional circuit complexity will be needed to model actual filters, where coupling springs generalize to transmission lines, and resonators must be modeled by circuits similar to that of Fig. 10.

3.3.1. A Two-Resonator HF-VHF Micromechanical Filter

Figure 14 shows the perspective-view schematic of a practical two-resonator micromechanical filter [18] capable of operation in the HF to VHF range. As shown, the filter consists of two μmechanical clamped-clamped beam resonators, coupled mechanically by a soft spring, all suspended 0.1 μm above the substrate. Conductive (polysilicon) strips underlie each resonator, the center ones serving as capacitive transducer electrodes positioned to induce resonator vibration in a direction perpendicular to the substrate, the flanking ones serving as tuning electrodes capable of voltage-controlled tuning of resonator frequencies, as governed by (13). The resonator-to-electrode gaps are determined by the thickness of a sacrificial oxide spacer during fabrication and can thus be made quite small (e.g., 0.1 μm or less) to maximize electromechanical coupling.

The filter is excited in a similar fashion to that described in the previous sub-section, with a dc-bias voltage V_P applied to the conductive mechanical network, and an ac signal applied to the input electrode, but this time through an appropriately valued source resistance R_Q that loads the Q of the input resonator to flatten the passband [18]. The output resonator of the filter must also see a matched impedance to avoid passband distortion, and the output voltage v_o is generally taken across this impedance. As will be seen in the next section, the required value of I/O port termination resistance can be tailored for different applications, and this can be advantageous when designing low noise transistor circuits succeeding the filter, since such circuits can then be driven by optimum values of source resistance to minimize noise figure [32].

From a signal flow perspective, the operation of the above filter can be briefly summarized as follows:

(1) An electrical input signal is applied to the input port and converted to an input force by the electromechanical transducer (which for the case of Fig. 14(a) is capacitive) that can then induce mechanical vibration in the x direction;

(2) mechanical vibration comprises a mechanical signal that is processed in the mechanical domain—specifically, the signal is rejected if outside the passband of the filter, and passed if within the passband; and

(3) the mechanically processed signal appears as motion of the output resonator and is re-converted to electrical energy at the output transducer, ready for processing by

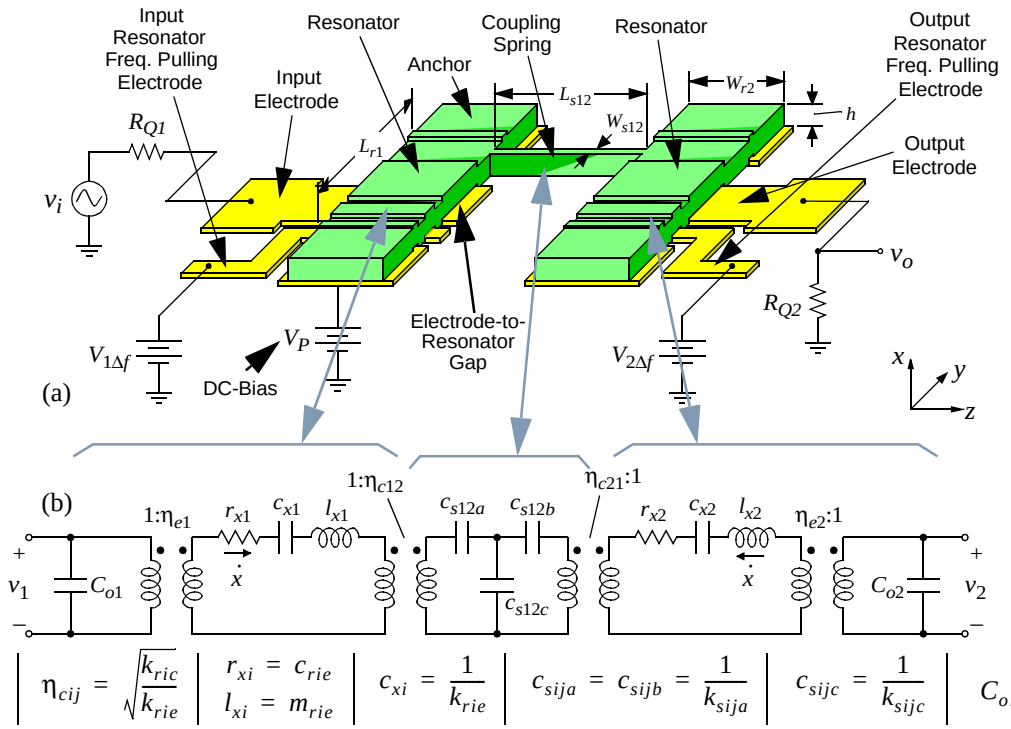

$$\eta_{ei} = \text{Eq. (20)} \quad \left| \quad \eta_{cij} = \sqrt{\frac{k_{ric}}{k_{rie}}} \quad \right| \quad \begin{matrix} r_{xi} = c_{rie} \\ l_{xi} = m_{rie} \end{matrix} \quad \left| \quad c_{xi} = \frac{1}{k_{rie}} \quad \right| \quad c_{sija} = c_{sijb} = \frac{1}{k_{sija}} \quad \left| \quad c_{sijc} = \frac{1}{k_{sijc}} \quad \right| \quad C_{oi} = \frac{\varepsilon_o W_r W_e}{d}$$

Fig. 14. (a) Perspective-view schematic of a symmetrical two-resonator VHF μmechanical filter with typical bias, excitation, and signal conditioning electronics. (b) Electrical equivalent circuit for the filter in (a) along with equations for the elements [18]. Here, m_{rie}, k_{rie}, and c_{rie} denote the mass, stiffness, and damping of resonator i at the beam center location, and η_e and η_c are turns ratios modeling electromechanical coupling at the inputs and mechanical impedance transformations at low velocity coupling locations.

subsequent transceiver stages.

From the above, the name "micromechanical signal processor" clearly suits this device. Details of the design procedure for micromechanical filters now follow.

3.3.2. HF-VHF Filter Design

As can be surmised from Fig. 12(b), the network topologies for the mechanical filters of this work differ very little from those of their purely electronic counterparts, and in principal, can be designed at the system-level via a procedure derived from well-known, coupled resonator ladder filter synthesis techniques. In particular, given the equivalent *LCR* element values for a prototype μmechanical resonator, it is possible to synthesize a mechanical filter entirely in the electrical domain, converting to the mechanical domain only as the last step. However, although possible, such a procedure is not recommended, since knowledge and ease of design in both electrical and mechanical domains can greatly reduce the effort required.

The design procedure for the two-resonator micromechanical filter of Fig. 14 can be itemized as follows:

(1) *Design and establish the μmechanical resonator prototype to be used, choosing necessary geometries for the needed frequency and insuring that enough electrode-to-resonator transducer coupling is provided to allow for predetermined termination resistor values.* For a given resonator, with predetermined values of W_r, h, W_e, V_P, and R_Q, this amounts to solving for the resonator length L_r and electrode-to-resonator gap spacing d that simultaneously satisfy (13), (25), and the equation for the needed termination resistor value [18], [29]:

$$R_{Qi} = \left(\frac{Q_i}{q_i Q_{fltr}} - 1\right)\frac{c_{rie}}{Q_i \eta_{ei}} = \left(\frac{Q_i}{q_i Q_{fltr}} - 1\right) R_{xi}\,, \qquad (26)$$

where Q_i is the uncontrolled quality factor of resonator i; $Q_{fltr} = f_o/B$ is the filter quality factor; q_i is a normalized q parameter obtained from a filter cookbook [31]; η_{ei} is given by (20); c_{rie} is given by (23), where the subscript e denotes the center location of the resonator over the electrode; and R_{xi} is the series motional resistance of end resonator i, given in (17). (Note that as mentioned previously, the resonators in a micromechanical filter are often designed to be identical, so the i subscript notation can actually be dropped from virtually all variables in (26), except q_i and R_{Qi}. The i subscripts are included for all variables just for completeness.) If the filter is designed symmetrically, with q_1=q_2, and with resonator Q's much greater than Q_{fltr}, the required value of the I/O port termination resistance for both end resonators becomes (dropping i subscripts)

$$R_Q \cong \frac{\sqrt{k_{re} m_{re}}}{q_1 Q_{fltr} \eta_e^2} = \frac{k_{re}}{\omega_o q_1 Q_{fltr} \eta_e^2}\,, \qquad (27)$$

where e denotes the center location of the resonator beam. Of the variables in (27), the electromechanical coupling factor η_e is often the most convenient parameter to adjust for a desired value of termination resistance. Given from (20) that $\eta_e \sim (V_P/d^2)$, termination impedance R_Q requirements and bias voltage V_P limitations often dictate the electrode-to-resonator gap spacing for a particular resonator design. This can be seen in Table 3, which summarizes the needed gap spacings to achieve various values of R_Q for microme-

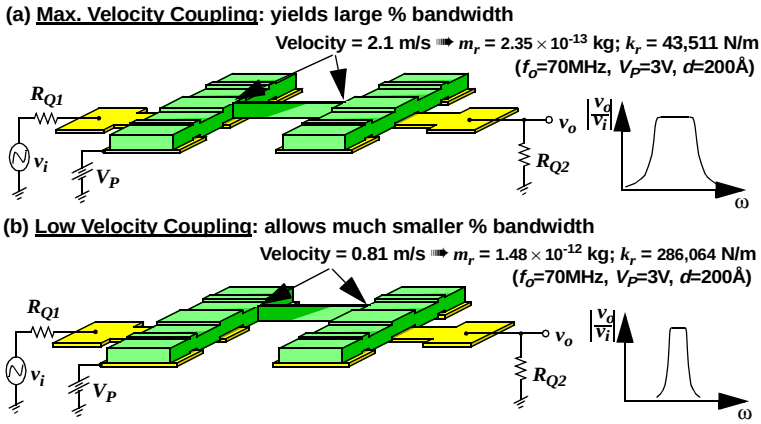

Fig. 15. Filter schematics showing (a) maximum velocity coupling to yield a large percent bandwidth and (b) low velocity coupling to yield a smaller percent bandwidth.

Table 3: Two-Resonator μMechanical Filter Electrode-to-Resonator Gap Spacing Design*

	Gap Spacing, d, for R_Q=				
Frequency	**300Ω**	**500Ω**	**1,000Ω**	**2,000Ω**	**5,000Ω**
70 MHz†	195Å	223Å	266Å	317Å	399Å
870 MHz‡	78Å	81Å	80Å	95Å	119Å

* Determined with Q=10,000, B=1.25MHz, V_P=10V.
† CCBeam, polysilicon, L_r=14.52μm, W_r=8μm, h=2μm.
‡ CCBeam, diamond, L_r=9.36μm, W_r=8μm, h=4μm.

chanical filters centered at 70 MHz and 870 MHz, and with Q=10,000, B=1.25MHz, and V_P=10V.

(2) *Choose a manufacturable value of coupling beam width W_{s12} and design coupling beam(s) corresponding to a "quarter-wavelength" of the filter center frequency.* Here, the coupling beam is recognized as an acoustic transmission line that can be made transparent to the filter when designed with quarter-wavelength dimensions [18], [23], [29]. For a flexural-mode coupling beam, neglecting rotational movements at the resonator attachment points, quarter-wavelength dimensions are achieved when the coupling beam width W_{s12} and length L_{s12} are chosen to satisfy the expression [29]

$$H_6 = \sinh\alpha\cos\alpha + \cosh\alpha\sin\alpha = 0, \qquad (28)$$

where $\alpha = L_{s12}(\rho W_{s12} h\omega^2/(EI_{s12}))^{0.25}$, $I_{s12} = W_{s12}h^3/12$, and needed dimensions are given in Fig. 14(a). Note that in choosing W_{s12} and L_{s12} to satisfy (28), the coupling beam stiffness k_{s12} is constrained to a particular value, given by [29]

$$k_{s12} = -\frac{EI_{s12}\alpha^3(\sin\alpha + \sinh\alpha)}{L_{s12}^3(\cos\alpha\cosh\alpha - 1)}. \qquad (29)$$

Note that this also constrains the ability to set the bandwidth of the filter via the coupling beam dimensions, and thus, necessitates an alternative method for setting bandwidth.

(3) *Determine the coupling location(s) on the resonators corresponding to the filter bandwidth of interest.* This procedure is based upon two important properties of this filter and the resonators comprising it: First, the filter bandwidth B is determined not by absolute values of stiffness, but rather by a ratio of stiffnesses (k_{s12}/k_{rc}), where the subscript c denotes the value at the coupling location; and second, the value of resonator stiffness k_{rc} varies with location (in particular, with location velocity) and so can be set to a desired value by simply choosing an appropriate coupling beam attachment point. Using (8), (10), (25), and (29), an expression that can be solved for the location l_c on the resonator beam where the coupling beam should be attached, can be written as

$$X_{mode}(l_c) = \left[2\pi B\frac{k_{12}}{k_{s12}}\rho W_r h\int_0^{L_r}[X(y')]^2 dy'\right]^{1/2}. \qquad (30)$$

Figure 15 illustrates how the choice of coupling beam attachment point can greatly influence the bandwidth of a mechanical filter. In Fig. 15(a), the coupling beam is attached at the highest velocity point, where the resonator presents its smallest stiffness, resulting in a very wide filter bandwidth. On the other hand, Fig. 15(b) depicts coupling at a lower velocity point closer to the resonator anchors, where the resonator presents a much higher stiffness, leading to a much smaller percent bandwidth, as dictated by (25). In effect, the bandwidth of the filter is set not by choosing the coupling beam stiffness k_{s12}, but rather by choosing an appropriate value of resonator stiffness k_{rc} to satisfy (25), given a k_{s12} constrained by quarter-wavelength design.

(4) *Generate a complete equivalent circuit for the overall filter and verify the design using a circuit simulator.* Figure 14(b) presents the equivalent circuit for the two-resonator micromechanical filter of Fig. 14(a) along with equations for the elements. As shown, each of the outside resonators are modeled via circuits such as shown in Fig. 10. The coupling beam actually operates as an acoustic transmission line, and thus, is modeled by a T-network of energy storage elements. Consistent with Fig. 10 and the discussion in item (3)

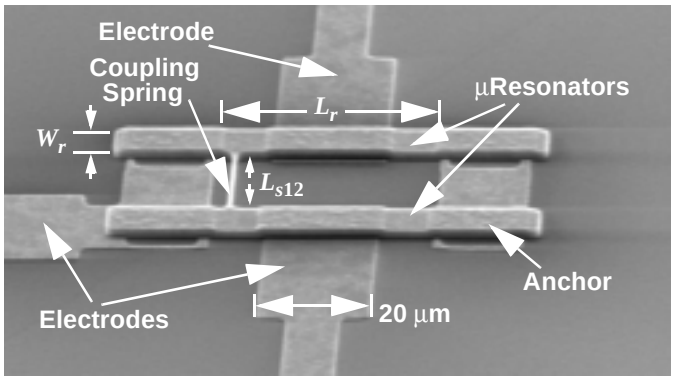

Fig. 16: SEM of a fabricated 7.81 MHz two-resonator micromechanical filter [18].

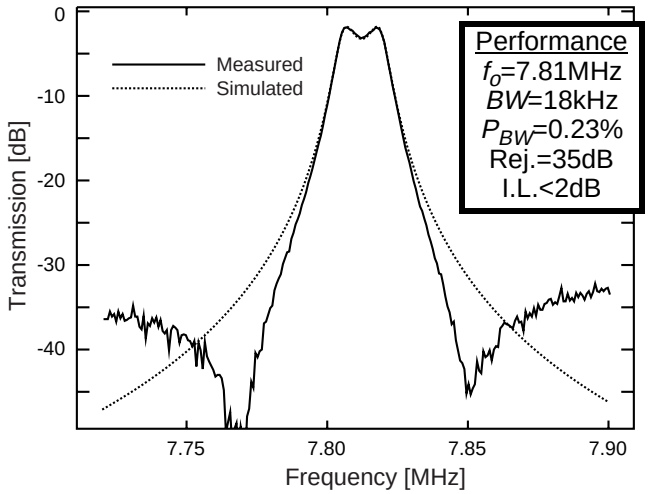

Fig. 17: Measured spectrum for a terminated 7.81 MHz μmechanical filter with excessive input/output shunt capacitance. Here, Q_{fltr}=435. [18]

above, transformers are used between the resonator and coupling beam circuits of Fig. 14(b) to model the velocity transformations that arise when attaching the coupling beams at locations offset from the center of the resonator beam. The whole circuit structure of Fig. 14(b) can be recognized as that of the *LC* ladder network for a bandpass filter.

Further details on the design of micromechanical filters can be found in the literature [18], [23], [29].

3.3.3. HF Micromechanical Filter Performance

Figure 16 presents the SEM of a symmetrical (i.e., R_{Q1}=R_{Q2}) 7.81 MHz micromechanical filter using the design of Fig. 14 and constructed of phosphorous-doped polycrystalline silicon [18]. The measured spectrum for a terminated version of this filter is shown in Fig. 17 (solid curve), showing a bandwidth of 18 kHz, which is very close to the design value. The insertion loss is only 1.8 dB, which is impressive for a bandpass filter with a percent bandwidth of 0.23% (Q_{fltr}=435) and which can be attributed to the high *Q* of the constituent μmechanical resonators. Designed and measured μmechanical filter characteristics are summarized in Table 4. It should be noted that although the analytical design calls for 19.6kΩ termination resistors, only 12.2kΩ resistors were used in the

Table 4: HF Micromechanical Filter Summary [18]

Parameter	Value*†‡		Units
	Des./Meas.	Simulated#	
Coupling Location, l_c	4.08	**4.48**	μm
Coupling Velocity, v_c	$0.12v_{max}$	$\mathbf{0.14v_{max}}$	m/s
Center Frequency, f_o	7.81	7.81	MHz
Freq. Modification Factor, κ	(0.87915) [0.9]	0.87915	—
Bandwidth, *B*	18	18	kHz
Percent Bandwidth, (B/f_o)	0.23	0.23	%
Passband Ripple, *PR*	1.5	1.5 [0.5]	dB
Insertion Loss, *IL*	1.8	1.8 [1.35]	dB
20dB Shape Factor,	2.31	[2.54]	—
Stopband Rejection, *SR*	35	—	dB
Sp.-Free Dynamic Range, *SFDR*	~78	~78	dB
Resonator *Q*	8,000	**6,000**	—
Structural Layer Thickness, *h*	1.9	1.9	μm
μRes. Beam Length, L_r	40.8	40.8	μm
μRes. Beam Width, W_r	8	8	μm
Coupling Beam Length, L_{s12}	20.35	20.35	μm
Needed L_{s12} for λ/4	(22.47)	—	μm
Coupling Beam Width, W_{s12}	0.75	0.75	μm
Coupling Beam Stiffness, k_{s12a}	(–82.8)	–82.8	N/m
Coupling Beam Stiffness, k_{s12c}	(113.4)	113.4	N/m
Resonator Mass @ I/O, m_{re}	(5.66×10^{-13})	5.66×10^{-13}	kg
Resonator Stiffness @ I/O, k_{re}	(1,362)	1,362	N/m
Resonator Mass @ l_c, m_{rc}	(3.99×10^{-11})	2.84×10^{-11}	kg
Resonator Stiffness @ l_c, k_{rc}	(96,061)	68,319	N/m
Integrated μRes. Stiffness, k_{reff}	(1,434)	1,434	N/m
Young's Modulus, *E*	150	150	GPa
Density of Polysilicon, ρ	2,300	2,300	kg/m^3
Electrode-to-μRes. Gap, d_o	1,300	1,300	Å
Gap d_o Adjusted for Depletion	(1,985)	1,985	Å
Electrode Width, W_e	20	20	μm
Filter DC-Bias, V_P	35	35	V
Freq. Pulling Voltage, $V_{\Delta f}$	0.12	0	V
Q-Control Resistors, R_Q	12.2 (19.6)	**14.5** [19.6]	kΩ

* Numbers in () indicate calculated or semi-empirical values.

† Bold faced numbers indicate significant deviations needed to match simulated curves with measured curves.

‡ Numbers in [] indicate values expected from an ideal simulation with no parasitics and perfect termination. The value for κ in the "Des./Meas." column was obtained via finite-element simulation using ANSYS.

\# Top 11 rows represent simulation outputs; the rest are used as inputs for simulation.

Table 5: HF μmechanical Filter Circuit Element Values for the Data of Table 4 [18]

Parameter	Value	Units
Coupling Location, l_c	4.48	μm
C_{o1}=C_{o2}	7.14	fF
l_{x1}=l_{x2}	5.66×10^{-13}	H
c_{x1}=c_{x2}	0.000734	F
r_{x1}=r_{x2}	4.62×10^{-9}	Ω
c_{s12a}=c_{s12b}	–0.0121	F
c_{s12c}	0.00882	F
η_{e1}=η_{e2}	1.20×10^{-6}	C/m
η_{c12}=η_{c21}	7.08	C/m

actual measurement to minimize phase lags caused by board-level parasitic capacitance.

In addition to the measured frequency response, Fig. 17 also presents a simulated spectrum (dotted line) using the equivalent circuit described by Fig. 14(b) with element values derived from the "Simulated" column of Table 4 and summarized in Table 5. This simulation attempts to mimic the measured frequency characteristic in the passband. As such, it includes shunt parasitic capacitors C_{Pn}=100fF at the input and output nodes to model board-level parasitics that interact with termination resistors R_{Qn} and generate increased passband ripple. It should be noted, however, that a few adjustments were necessary to attain the degree of matching shown, with the more important adjustments indicated in boldface font. In particular, note that the target gap spacing of 1,300Å was not used to generate the "Simulated" column in Table 4, nor the values in Table 5. Rather, a larger gap spacing of 1,985Å was used that accounts for depletion in the resonator beam induced by the V_P-induced electric field between the non-degenerately-doped n-type beam and the n-type electrode [18]. This value of gap spacing was semi-empirically determined by matching measured plots of resonator f_o vs. V_P with simulations based on (13), using d_o and κ as fitting parameters.

In addition, as indicated in boldface in Table 4, the coupling location l_c was adjusted to match bandwidths, and the resonator Q and the filter termination resistance R_Q were adjusted to match the measured insertion loss. In particular, the value of R_Q needed to match the simulated insertion loss and passband ripple was 14.5kΩ, not the 12.2kΩ actually used for the measurement.

The l_c adjustment is not unreasonable, since the coupling beam has a finite width of 0.75 μm, and the exact coupling location is not necessarily at the center of the coupling beam, but could be anywhere along its finite width. Furthermore, torsional motions of the coupling beam can also influence the actual mechanical coupling, thus, changing the effective l_c. The adjustment in Q seen in Table 4 is also plausible, since a small number of resonators in the filter fabrication run exhibited lower Q than the 8,000 measured in Fig. 7. The small deviation in R_Q also should not be alarming, given some uncertainty in the actual gap distance for this process.

Note that although the simulation matches the measurement very well in the passband, it deviates substantially in its transition to the stopband. In particular, the measured curve features loss poles not modeled by the theory of Section 3.3.2 that substantially improve the shape factor of the filter. The loss poles in Fig. 17 result largely from action of a feedthrough capacitor $C_{P(fd)}$ that connects the input ad output electrodes, and that influences the filter frequency characteristic in a similar fashion to the introduction of loss poles via bridging capacitors in crystal filter design [33]. In the present experiment, $C_{P(fd)}$ is actually a parasitic element; i.e., loss poles were introduced inadvertently. For fully integrated filters, in which μmechanics and circuits are fabricated side-by-side on a single-chip, parasitic capacitors are expected to be much smaller. In this case, the feedthrough capacitor $C_{P(fd)}$ can then be purposefully designed into the filter if loss poles are desired.

3.4. Micromechanical Mixer-Filters

As indicated by (3), the voltage-to-force transducer used by the described resonators is nonlinear, relating input force F_d to input voltage $(v_e–v_b)$ by a square law. When v_b=V_P, this nonlinearity is suppressed, leading to a dominant force that is linear with v_e given by the second term of (5). If, however, signal inputs are applied to both v_e and v_b, a square law mixer results. In particular, if an RF signal v_{RF}=$V_{RF}\cos\omega_{RF}t$ is applied to electrode *e*, and a local oscillator signal v_{LO}=$V_{LO}\cos\omega_{LO}t$ to electrode *b*, then (3) contains the term

$$F_d = \ldots + \frac{1}{2}V_{RF}V_{LO}\frac{\partial C}{\partial x}\cos(\omega_{RF}-\omega_{LO})t + \ldots \qquad (31)$$

which clearly indicates a mixing of *voltage* signals v_{RF} and v_{LO} down to a *force* signal at frequency ω_{IF}=$(\omega_{RF}–\omega_{LO})$. If the above transducer is used to couple into a μmechanical filter with a passband centered at ω_{IF}, an effective mixer-filter device results that provides both a mixer and filtering function in one passive, micromechanical device.

Figure 18(a) presents the schematic for a symmetrical μmechanical mixer-filter [34], showing the bias and input scheme required for down-conversion and equating this device to a system-level functional block. As shown, since this device provides filtering as part of its function, the overall mechanical structure is exactly that of a μmechanical filter. The only differences are the applied inputs and the use of a non-conductive coupling beam to isolate the IF port from the LO. Note that if the source providing V_P to the second resonator is ideal (with zero source resistance) and the series resistance in the second resonator is small, LO signals feeding across the coupling beam capacitance are shunted to ac ground before reaching the IF port. In reality, finite resistivity in the resonator material allows some amount of LO-to-IF leakage.

The mixer conversion gain/loss in this device is determined primarily by the relative magnitudes of the dc-bias V_P applied to the resonator and the local oscillator amplitude V_{LO}. Using (31), assuming R_Q resistors given by (26), and with the recognition that the filter structure presents a large input impedance to both v_{RF} and v_{LO} (since their frequencies are off-resonance), the expression for conversion gain/loss takes the form

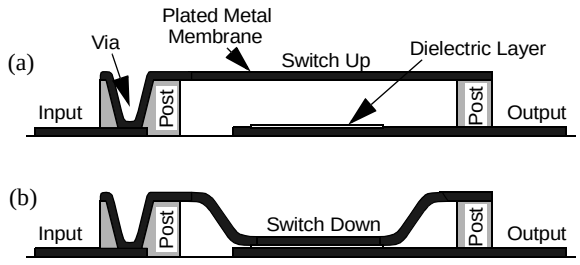

Fig. 19: Cross-sectional schematics of a typical μmechanical switch: (a) Switch up. (b) Switch down [35].

$$G_{conv} = \frac{1}{L_{conv}} = \frac{V_{LO}}{V_P} \rightarrow 20\log\left[\frac{V_{LO}}{V_P}\right] \text{ [dB]}. \qquad (32)$$

Note that conversion gain is possible if $V_{LO} > V_P$.

The SSB noise figure for this device derives from a combination of mixer conversion loss, filter insertion loss, and an additional 3dB that accounts for noise conversion from two bands (RF and image) to one [11], and can be expressed as

$$NF = L_{conv}\big|_{\text{dB}} + L_{fltr}\big|_{\text{dB}} + 3 \quad \text{[dB]}, \qquad (33)$$

where $L_{fltr}|_{\text{dB}}$ is the filter insertion loss in dB. Possible values might be $L_{conv}|_{\text{dB}}$=0dB (with V_{LO}=V_P) and $L_{fltr}|_{\text{dB}}$=0.5dB, leading to *NF*=3.5dB—very good calculated performance for a combined mixer and filter using passive components.

3.5. Micromechanical Switches

The mixer-filter device described above is one example of a μmechanical circuit that harnesses nonlinear device properties to provide a useful function. Another very useful mode of operation that further utilizes the nonlinear nature of the device is the μmechanical switch. Figure 19 presents an operational schematic for a single-pole, single-throw μmechanical switch [35], seen to have a structure very similar to that of the previous resonator devices: a conductive beam or membrane suspended above an actuating electrode. The operation of the switch of Fig. 19 is fairly simple: To achieve the "on-state", apply a sufficiently large voltage across the beam and electrode to pull the beam down and short it (in either a dc or ac fashion) to the electrode.

In general, to minimize insertion loss, the majority of switches use metals as their structural materials. It is their metal construction that makes μmechanical switches so attractive, allowing them to achieve "on-state" insertion losses down to 0.1 dB—much lower than FET transistor counterparts, which normally exhibit ~2 dB of insertion loss. In addition to exhibiting such low insertion loss, μmechanical switches are extremely linear, with *IIP3*'s greater than 66 dBm [8], and can be designed to consume no dc power (as opposed to FET switches, which sink a finite current when activated).

Chapter *** in this book covers micromechanical switches in much greater detail.

4. RF Receiver Front-End Architectures Using MEMS

Having surveyed a subset of the mechanical circuits most useful for communication applications, we now consider methods by which these circuits are best incorporated into communications sub-systems. Three approaches to using micromechanical vibrating resonators are described in order of increasing performance enhancement: (1) direct replacement of off-chip high-*Q* passives; (2) use of an RF channel select architecture using a large number of high-*Q* micromechanical resonators in filter banks and switchable networks; and (3) use of an all-mechanical RF front-end.

In proposing these architectures, certain liberties are taken in an attempt to account for potential advances in micromechanical resonator technology. For example, in the RF channel-select architecture, μmechanical circuits are assumed to be able to operate at UHF with *Q*'s on the order of 10,000. Given that TFR's already operate at UHF (but with *Q*'s of 1,000), and 100 MHz free-free beam μmechanical resonators presently exhibit *Q*'s around 8,000, the above assumed performance values may, in fact, not be far away. At any rate, the rather liberal approach taken in this section is largely beneficial, since it better conveys the potential future impact of MEMS technology, and provides incentive for further advancements in this area. Nevertheless, in order to keep in check the enthusiasm generated here, assumed performances in this section are briefly re-evaluated in the next, with an eye towards practical implementation issues.

4.1. Direct Replacement of Off-Chip High-*Q* Passives

Perhaps the most direct way to harness μmechanical circuits is via direct replacement of the off-chip ceramic, SAW, and crystal resonators used in RF preselect and image reject filters, IF channel-select filters, and crystal oscillator references. A schematic depicting this approach was shown previously in Fig. 1, and now in a condensed form in Fig. 20. In addition to high-*Q* components, Figs. 1 and 20 also show the use of other MEMS-based passive components, such as medium-*Q* micro-

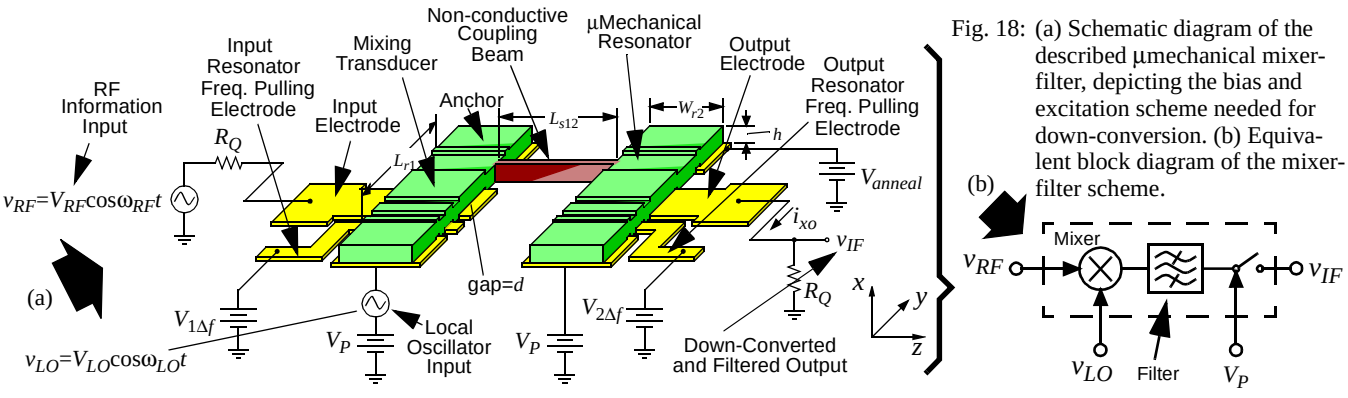

Fig. 18: (a) Schematic diagram of the described μmechanical mixer-filter, depicting the bias and excitation scheme needed for down-conversion. (b) Equivalent block diagram of the mixer-filter scheme.

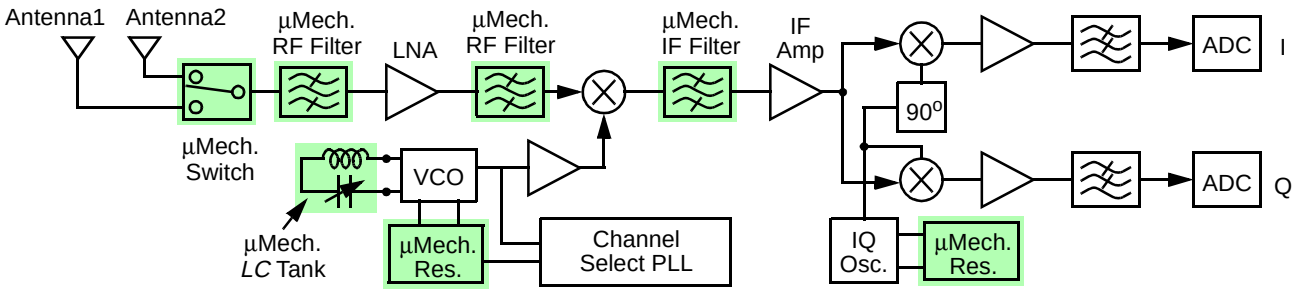

Fig. 20: System block diagram of a super-heterodyne receiver architecture showing potential replacements via MEMS-based components. (On-chip µmechanics are shaded.)

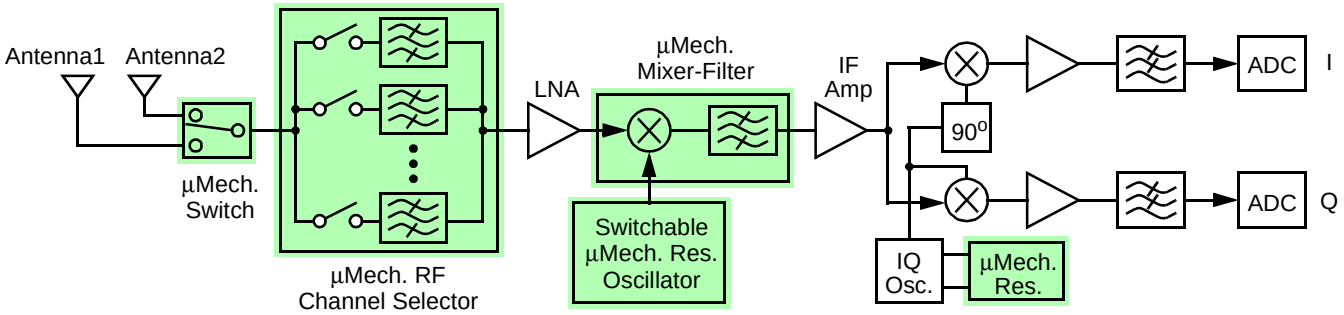

Fig. 21: System block diagram for an RF channel-select receiver architecture utilizing large numbers of micromechanical resonators in banks to trade *Q* for power consumption. (On-chip µmechanics are shaded.)

machined inductors and tunable capacitors [36] used in VCO's and matching networks, as well as low-loss (~0.1dB) µmechanical switches [35] that not only provide enhanced antenna diversity, but that can also yield power savings by making TDD (rather than FDD) more practical in future transceivers.

Of course, the main benefits from the above approach to using MEMS are size reduction and, given the potential for integration of MEMS with transistor circuits, the ability to move more components onto the silicon die. A limited number of performance benefits also result from replacement of existing high-*Q* passives by µmechanical ones, such as the ability to tailor the termination impedances required by RF and IF filters (c.f., Table 3). Such impedance flexibility can be beneficial when designing low-noise amplifiers (LNA's) and mixers in CMOS technology, which presently often consume additional power to impedance match their outputs to 50Ω off-chip components. If higher impedances can be used, for example at the output of an LNA, significant power savings are possible. As an additional benefit, since the source impedance presented to the LNA input is now equal to R_Q, it can now be tailored to minimize noise figure (*NF*).

Although beneficial, the performance gains afforded by mere direct replacement by MEMS are quite limited when compared to more aggressive uses of MEMS technology. More aggressive architectures will now be described.

4.2. An RF Channel-Select Architecture

To fully harness the advantages of µmechanical circuits, one must first recognize that due to their micro-scale size and zero dc power consumption, µmechanical circuits offer the same system complexity advantages over off-chip discrete components that planar IC circuits offer over discrete transistor circuits. Thus, to maximize performance gains, µmechanical circuits should be utilized on a massive scale.

Perhaps one of the simplest ways to harness the small size of micromechanical circuits is to add multi-band reconfigurability to a transceiver by adding a preselect and image reject filter for each communication standard included. Due to the small size of micromechanical filters, this can be done with little regard to the overall size of the transceiver.

Although the above already greatly enhances the capability of today's wireless transceivers, it in fact only touches upon a much greater potential for performance enhancement. In particular, it does not utilize micromechanical circuits to their fullest complexity. Figure 21 presents the system-level block diagram for a possible receiver front-end architecture that takes full advantage of the complexity achievable via µmechanical circuits. The main driving force behind this architecture is power reduction, attained in several of the blocks by trading power for high selectivity (i.e., high-*Q*). The key power saving blocks in Fig. 21 are now described.

4.2.1. Switchable RF Channel Select Filter Bank

If channel selection (rather than pre-selection) were possible at RF frequencies (rather than just at IF), then succeeding electronic blocks in the receive path (e.g., LNA, mixer) would no longer need to handle the power of alternate channel interferers. Thus, their dynamic range can be greatly relaxed, allowing substantial power reductions. In addition, the rejection of adjacent channel interferers also allows reductions in the phase noise requirements of local oscillator (LO) synthesizers, providing further power savings.

To date, RF channel selection has been difficult to realize via present-day technologies. In particular, low-loss channel selection at RF would require tunable resonators with *Q*'s in the thousands. Unfortunately, however, high-*Q* often precludes tunability, making RF channel selection via a single RF filter a very difficult prospect.

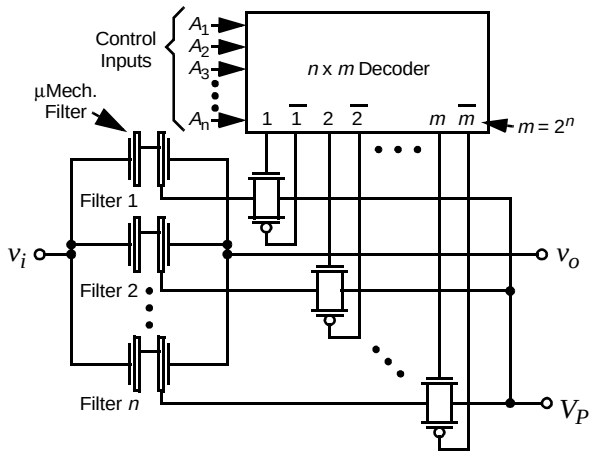

Fig. 22: System/circuit diagram for an RF channel-select micromechanical filter bank.

On the other hand, it is still possible to select individual RF channels via many non-tunable high-*Q* filters, one for each channel, and each switchable by command. Depending upon the standard, this could entail hundreds or thousands of filters—numbers that would be absurd if off-chip macroscopic filters are used, but that may be perfectly reasonable for microscale, passive, µmechanical filters, such as described in Section 3.3.

Figure 22 presents one fairly simple rendition of the key system block that realizes the desired RF channel selection. As shown, this block consists of a bank of µmechanical filters with all filter inputs connected to a common block input and all outputs to a common block output, and where each filter passband corresponds to a single channel in the standard of interest. In the scheme of Fig. 22, a given filter is switched on (with all others off) by decoder-controlled application of an appropriate dc-bias voltage to the desired filter. (Recall from (3) and (7) that the desired force input and output current are generated in a µmechanical resonator only when a dc-bias V_P is applied; i.e., without V_P, the input and output electrodes are effectively open-circuited.)

The potential benefits afforded by this RF channel selector can be quantified by assessing its impact on the LNA linearity specification imposed by the IS-98-A interim standard for CDMA cellular mobile stations [37]. In this standard, the required IIP3 of the LNA is set mainly to avoid desensitization in the presence of a single tone (generated by AMPS [37]) spaced 900kHz away from the CDMA signal center frequency. Here, reciprocal mixing of the local oscillator phase noise with the 900kHz offset single tone and cross-modulation of the single tone with leaked transmitter power outputs dictate that the LNA IIP3 exceeds +7.6dBm [37]. However, if an RF channel select filter bank such as shown in Fig. 22 precedes the LNA and is able to reject the single tone by 40dB, the requirement on the LNA then relaxes to IIP3 ≤–29.3dBm (assuming the phase noise specification of the local oscillator is *not* also relaxed). Given the well-known noise and linearity versus power trade-offs available in LNA design [38], [39], such a relaxation in IIP3 can result in nearly an order of magnitude reduction in power. In addition, since RF channel selection relaxes the overall receiver linearity requirements, it may become possible to put more gain in the LNA to suppress noise figure (*NF*) contributions from later stages, while relaxing the required *NF* of the LNA itself, leading to further power savings.

Turning to oscillator power, if the single tone interferer is attenuated to 40dB, then reciprocal mixing with the local oscillator is also greatly attenuated, allowing substantial reduction in the phase noise requirement of the local oscillator. Requirement reductions can easily be such that on-chip solutions to realization of the receive path VCO (e.g., using spiral inductors and pn-diode tunable capacitors) become plausible.

4.2.2. Switchable Micromechanical Resonator Synthesizer

Although the µmechanical RF channel-selector described above may make possible the use of existing on-chip technologies to realize the receive path VCO, this approach is not recommended, since it denies the system from achieving much greater power reduction factors that may soon be available through MEMS technology. In particular, given that power and *Q* can often be interchanged when designing for a given oscillator phase noise specification, a better approach to implementing the VCO would be to use µmechanical resonators (with orders of magnitude higher *Q* than any other on-chip tank) to set the VCO frequency. In fact, with *Q*'s as high as achievable via µmechanics, the basic design methodologies for oscillators must be re-evaluated. For example, in the case where the oscillator and its output buffer contribute phase noise according to Leeson's equation [40], where the $1/f^2$-to-white phase noise corner occurs at $(f_o/(2Q))$, a tank Q>1,500 is all that would be required to move the $1/f^2$-to-white phase noise corner close enough to the carrier that only white phase noise need be considered for CDMA cellular applications, where the phase noise power at frequency offsets from 285kHz to 1515kHz is most important. If only white noise is important, then only the output buffer noise need be minimized, and sustaining amplifier noise may not even be an issue. If so, the power requirement in the sustaining amplifier might be dictated solely by loop gain needs (rather than by phase noise needs), which for a µmechanical resonator-based VCO with R_x~40Ω, L_x~84µH, and C_x~0.5fF, might be less than 1mW.

To implement a tunable local oscillator synthesizer, a switchable bank is needed, similar to that of Fig. 22 but using µmechanical resonators, not filters, each corresponding to one of the needed LO frequencies, and each switchable into or out of the oscillator sustaining circuit. Note that because µmechanical resonators are now used in this implementation, the *Q* and thermal stability (with compensation electronics) of the oscillator may now be sufficient to operate without the need for locking to a lower frequency crystal reference. The power savings attained upon removing the PLL and prescaler electronics needed in past synthesizers can obviously be quite substantial. In effect, by implementing the synthesizer using µmechanical resonators, synthesizer power consumption can be reduced from the ~90mW dissipated by present-day implementations using medium-*Q L* and *C* components [41], to something in the range of only 1-4 mW. Again, all this is attained using a circuit topology that would seem absurd if only macroscopic high-*Q* resonators were available, but that becomes plausible in the

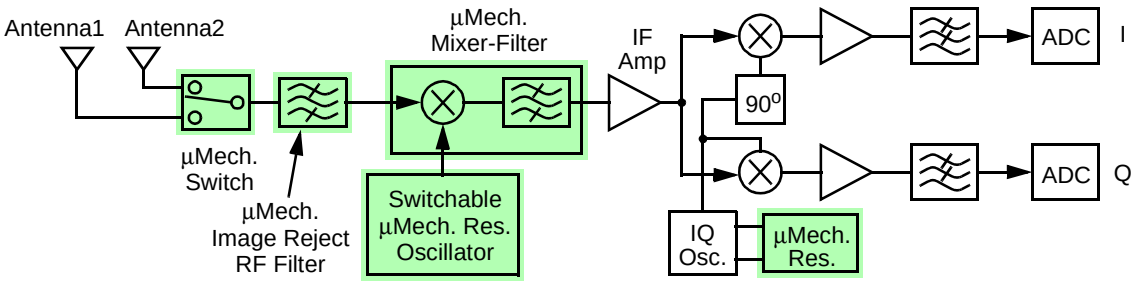

Fig. 23: System-block diagram for an all-MEMS RF front-end receiver architecture. (On-chip μmechanics are shaded.)

micromechanical arena.

4.2.3. Micromechanical Mixer-Filter

The use of a μmechanical mixer-filter in the receive path of Fig. 21 eliminates the dc power consumption associated with the active mixer normally used in present-day receiver architectures. This corresponds to a power savings on the order of 10-20 mW. In addition, if multiple input electrodes (one for RF, one for matching) are used for the mixer-filter, the RF input can be made to appear purely capacitive to the LNA (i.e., at the RF frequency), and the LNA would no longer require a driver stage to match a certain impedance. Rather, an inductive load can be used to resonate the capacitance, as in [38], allowing power savings similar to that discussed in Section 4.1.

4.3. An All-MEMS RF Front-End Receiver Architecture

In discussing the above MEMS-based architecture, one very valid question may have arisen: If μmechanical filters and mixer-filters can truly post insertion losses consistent with their high-*Q* characteristics, then is an LNA really required at RF frequencies? It is this question that inspires the receiver architecture shown in Fig. 23, which depicts a receive path comprised of a relatively wideband image reject μmechanical RF filter followed immediately by a narrowband IF mixer-filter that then feeds subsequent IF electronics. The only active electronics operating at RF in this system are those associated with the local oscillator, which if it uses a bank of μmechanical resonators, may be able to operate at less than 1 mW. If plausible, the architecture of Fig. 23 clearly presents enormous power advantages, eliminating completely the power consumption of the LNA and active mixer of Fig. 20—a total power savings on the order of 40mW—and together with the micromechanical LO, substantially increasing mobile phone standby times.

To assess the plausibility of this all-MEMS front-end, one can determine whether or not this scheme yields a reasonable noise figure requirement at the input node of the IF amplifier in Fig. 23. An expected value for RF image reject filter insertion loss is IL~0.2dB, assuming that three resonators are used, each with Q=5,000. Using the value for mixer-filter noise figure NF_{mf}=3.5dB projected in Section 3.4, the total combined noise figure NF_{f+mf}=3.7dB. Given IS-98-A's requirement that the receiver noise figure $NF_{RX}\leq$7.8dB (with a 2dB conservative design buffer), the needed value at the IF amplifier input is $NF_{IF}\leq$4.1dB, which can be reasonable if the IF amplifier gain can be increased to suppress the noise of succeeding stages. IF-baseband strips for GSM with NF~3.8dB are, in fact, already available [42].

Although the all-MEMS front-end architecture of Fig. 23 may at first seem the most preposterous of the bunch, early versions of the primary filtering and mixing devices required for its implementation have already been demonstrated. In particular, TFR image-reject filters have been demonstrated at UHF frequencies with insertion losses of less than 3dB [19]. It should be noted, however, that the first demonstrated mixer-filter based on polysilicon clamped-clamped beam μmechanical resonators achieved NF_{mf}=15dB [34]—quite worse than the 3.5dB used in the above calculation, and in fact, a value that precludes the use of the architectures shown in Fig. 23. It is not unreasonable, however, to expect that future renditions of mixer-filters, perhaps using more appropriate resonators (e.g., higher Q free-free beams, rather than clamped-clamped beams), might be able to achieve the projected 3.5dB.

5. An RF Transmitter Architecture Using MEMS

Due to a lack of sufficient in-band power handling capability, very little consideration has been given to date to the possibility of using μmechanical resonators in the transmit path. However, research efforts are presently underway to remedy this, and if successful, equally compelling MEMS-based transmit architectures can also be proposed.

Figure 24 depicts one rendition, in which an RF channel-selector is placed after the power amplifier (PA) in the transmit path. This channel selector might utilize a similar circuit as that of Fig. 22, but using μmechanical resonators with sufficient power handling capability. Assuming for now that such devices are possible, this transmit topology could provide enormous power savings. In particular, if a high-*Q*, high-power filter with less than 1dB of insertion loss could follow the PA, cleaning all spurious outputs, including those arising from spectral regrowth, then more efficient PA designs can be utilized, despite their nonlinearity. For example, a PA previously restricted by linearity considerations to 30% efficiency in present-day transmitter architectures, may now be operable closer to its maximum efficiency, perhaps 50%. For a typical transmit power of 600mW, this efficiency increase corresponds to 800mW of power savings. If a more efficient PA topology could be used, such as Class E, with theoretical efficiencies approaching 100%, the power savings could be much larger.

In addition to the MEMS-based channel-select RF filter bank, the architecture of Fig. 24 also features a micromechanical upconverter that uses a mixer-filter device, such as described in Section 3.4, to upconvert and filter the information signal before directing it to the power amplifier.

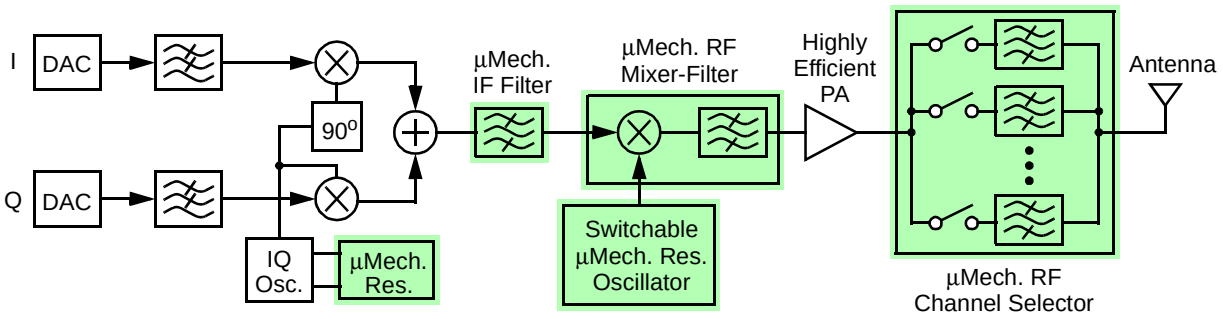

Fig. 24: RF channel-select transmitter architecture, possible only if high power µmechanical resonators can be achieved. Here, on-chip µmechanical blocks are shaded, and the PA is not necessarily implemented on-chip.

6. Research Issues

As stated at the beginning of Section 4, the transceiver architectures described above rely to some extent on performance characteristics not yet attained by µmechanical resonators, but targeted by ongoing research efforts. Specifically, µmechanical devices with the following attributes have been assumed: (1) adequate *Q* at UHF frequencies; (2) sufficient linearity and power handling capability; (3) usable port impedances; and (4) massive scale integration methods.

6.1. Frequency and *Q*

As previously mentioned, since TFR's can already operate in the 3-7 GHz range with *Q*'s of ~1,000, vibrating micromechanical high-*Q* tanks operating at UHF already exist. However, although their ~200 µm diameters are much smaller than corresponding dimensions on macroscopic counterparts, TFR's are still much larger than the micromechanical beams described in Section 3, which can have lengths less than 10 µm at UHF. Since tiny size is paramount in many of the proposed micromechanical architectures of Section 4 and 5, especially those calling for banks of numerous high-*Q* filters or resonators, the ultimate frequency range of micromechanical beam resonators is of great interest. Table 1 of Section 3.2 showed that from a purely geometric perspective, the frequencies required by the architectures of Section 4, from 10 MHz to 2.5 GHz, are reasonable for beam elements. Geometry, however, is only one of many important considerations. Indeed, the applicable frequency range of micromechanical resonators will also be a function of several other factors, including:

(1) quality factor, which may change with frequency for a given material, depending upon frequency-dependent energy loss mechanisms [43];

(2) linearity and power handling ability, which may decrease as the size of a given resonator decreases [18];

(3) series motional resistance R_x (c.f., Fig. 14), which must be minimized to allow impedance matching with other transceiver components and to alleviate filter passband distortion due to parasitics [17], [44], [45];

(4) absolute and matching tolerances of resonance frequencies, which will both be functions of the fabrication technology and of frequency trimming or tuning strategies [46]; and

(5) stability of the resonance frequency against temperature variations, mass loading, aging, and other environmental phenomena.

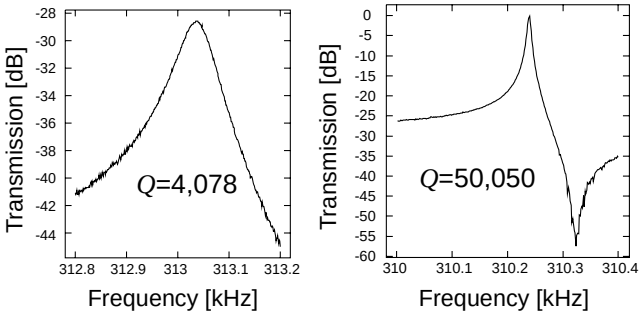

Fig. 25: Measured transconductance spectra for (a) a $POCl_3$-doped resonator and (b) an implant-doped version, both after furnace annealing.

Table VI: Doping Recipes

$POCl_3$	Implant
(i) Deposit 2 µm LPCVD fine-grained polysilicon @ 588°C (ii) Dope 2.5 hrs. @ 950°C in $POCl_3$ gas (iii) Anneal for 1 hr. @ 1100°C in N_2 ambient	(i) Deposit 1 µm LPCVD fine-grained polysilicon @ 588°C (ii) Implant phosphorous: Dose=10^{16} cm^{-2}, Energy=90 keV (iii) Deposit 1 µm LPCVD fine-grained polysilicon @ 588°C (iv) Anneal for 1 hr. @ 1100°C in N_2 ambient

Each of the above phenomena are currently under study. In particular, assuming adequate vacuum can be achieved, the ultimate quality factor will be strongly dependent upon the material type, and even the manufacturing process. For example, surface roughness or surface damage during fabrication may play a role in limiting quality factor. In fact, preliminary results comparing the quality factor achievable in diffusion-doped polysilicon structures (which exhibit substantial pitting of the poly surface) versus implant-doped ones, indicate that the latter exhibit almost an order of magnitude higher *Q* at frequencies near 10 MHz. Figure 25 presents measured transconductance spectra for two comb-driven folded-beam micromechanical resonators fabricated in the same polycrystalline material, but doped differently—one $POCl_3$-doped, the other phosphorous implant-doped—using the process sequences summarized in Table VI [46]. The difference in *Q* is

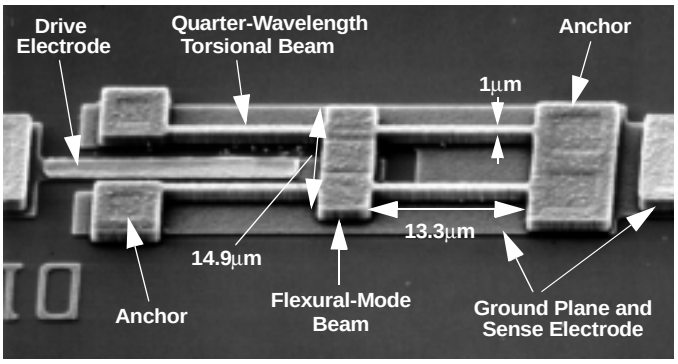

Fig. 26: SEM of a free-free beam virtually levitated micromechanical resonator with relevant dimensions for f_o=71 MHz.

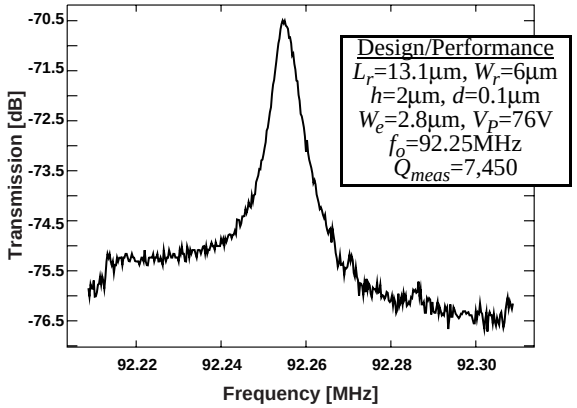

Fig. 27: Frequency characteristic for a fabricated 92.25 MHz free-free beam micromechanical resonator.

very intriguing, and is consistent with a surface roughness-dependent dissipation mechanism.

From a design perspective, one *Q*-limiting loss mechanism that becomes more important with increasing frequency is loss to the substrate through anchors. The frequency dependence of this mechanism arises because the stiffness of a given resonator beam generally increases with resonance frequency, giving rise to larger forces exerted by the beam on its anchors during vibration. As a consequence, more energy per cycle is radiated into the substrate via the anchors. Anti-symmetric resonance designs, such as balanced tuning forks, could prove effective in alleviating this source of energy loss.

Alternatively, anchor loss mechanisms can be greatly alleviated by using "anchor-less" resonator designs, such as shown in Fig. 26. This recently demonstrated device utilizes a free-free beam (i.e., xylophone) resonator suspended by four torsional supports attached at flexural node points. By choosing support dimensions corresponding to a quarter-wavelength of the free-free beam's resonance frequency, the impedance presented to the beam by the supports can be effectively nulled out, leaving the beam virtually levitated and free to vibrate as if it had no supports [11]. Figure 27 presents the frequency characteristic for a 92.25 MHz version of this μmechanical resonator, showing a *Q* of nearly 8,000—still plenty for channel-select RF applications. (Note that the excessive loss in the spectrum of Fig. 27 is an artifact of improper impedance matching between the resonator output and the measurement apparatus. In addition, this resonator used a conservative electrode-to-resonator gap spacing of d~2,000Å, so a rather large V_P was needed to provide a sufficient output level.)

What loss mechanisms await at GHz frequencies for flexural-mode resonators is, as yet, unknown. In particular, there is concern that frequency-dependent material loss mechanisms may cause *Q* to degrade with increasing frequency. Again, however, *Q*'s of over 1,000 at UHF (and beyond) have already been achieved via thin-film bulk acoustic resonators based on longitudinal resonance modes and piezoelectric structural materials. It is hoped that μmechanical resonators based on chemical vapor deposited (CVD) materials can retain *Q*'s of at least 8,000 at similar frequencies.

6.2. Linearity and Power Handling

Macroscopic high-*Q* filters based on ceramic resonator or SAW technologies are very linear in comparison with the transistor blocks they interface with in present-day transceivers. As a result, their contributions to the total IIP3 budget can generally be ignored in the majority of designs. In scaling the sizes of high-*Q* filtering devices to the micro-scale, however, linearity considerations must now be reconsidered, since past experience often says that the smaller the device, the less power it can handle.

For the capacitively-driven μmechanical resonator of Fig. 4, an approximate expression for the magnitude of the in-band force component at ω_o arising from third order intermodulation of two out-of-band interferers at $\omega_1=\omega_o+\Delta\omega$ and $\omega_2=\omega_o+2\Delta\omega$ can be derived by considering nonlinearities in the input capacitive transducer. Assuming that resonator displacements are small enough that stiffening nonlinearity can be neglected, such a derivation yields [18]

$$F_{IM_3} = V_i^3 \cdot \left\{ \frac{1}{4}\frac{(\varepsilon_o A_o)^2}{d_o^5}\frac{V_P}{k_{reff}}[2\Theta_1+\Theta_2] + \frac{3}{4}\frac{(\varepsilon_o A_o)^3}{d_o^8}\frac{V_P^3}{k_{reff}^2}\Theta_1[\Theta_1+2\Theta_2] + \frac{3}{2}\frac{(\varepsilon_o A_o)^4}{d_o^{11}}\frac{V_P^5}{k_{reff}^3}\Theta_1^2\Theta_2 \right\} \quad (34)$$

where $\Theta_1=\Theta(\omega_1)$, $\Theta_2=\Theta(\omega_2)$, and

$$\Theta(\omega) = \frac{1}{\left|1-(\omega/\omega_{u3dB})^2 + j\omega/(Q\omega_{u3dB})\right|}, \quad (35)$$

where $\omega_{u3dB}=\omega_o+B/2$ is the 3dB frequency at the upper edge of the filter passband. Equating (34) with the in-band force component (i.e., the second term of (5)), then solving for V_i, the IIP3 for a 70MHz μmechanical resonator is found to be around 12dB [18]. This is adequate for virtually all receive path functions, except for those in standards that allow simultaneous transmit and receive (such as CDMA), where the RF preselect filter is required to reject out-of-band transmitter outputs to alleviate cross-modulation phenomena [37]. For such situations, at least at present, a more linear filter must precede the filter bank of Fig. 22 if cross-modulation is to be sufficiently suppressed. This additional filter, however, can now have a very wide bandwidth, as it has no other purpose than to reject transmitter outputs. Thus, it may be realizable with very little insertion loss using on-chip (perhaps micromachined) inductor

and capacitor technologies [8].

It should be noted that the above hindrances exist mainly for systems using simultaneous transmit and receive. Burst mode, quasi-time-duplexed systems, such as GSM, should be able to use the micromechanical RF channel-selector by itself, without the need for a transmit reject filter.

It should also be mentioned that higher power handling micromechanical resonators are also presently being investigated. Among approaches being taken are the use of alternative geometries (e.g., no longer flexural mode) and the use of alternative transduction (e.g., piezoelectric, magnetostrictive). Such research efforts are aimed at not only out-of-band transmit power rejection, but on in-band handling of transmit power, as well, with a goal of realizing the RF channel-select transmit architecture described in Section 5.

6.3. Resonator Impedance

Thin-film bulk acoustic resonators can already impedance match to conventional antennas, so if their frequency, *Q*, yield, size, and integration capacity are adequate for a given architecture (e.g., the all-MEMS architecture of Section 4), then they present a very good solution. If higher *Q* is needed, however, then μmechanical resonators may be better suited for the given application. From Table 3, RF μmechanical filters should be able to match to 300Ω impedances, provided their electrode-to-resonator gaps can be made down to d~80Å. Since electrode-to-resonator gaps are achieved via a process very similar to that used to achieve MOS gate oxides [18], such gaps are not unreasonable. However, device linearity generally degrades with decreasing d, so practical designs must balance linearity with impedance requirements [18].

In cases where linearity issues constrain the minimum d to a value larger than that needed for impedance matching (assuming a fixed V_P), several μmechanical filters with identical frequency characteristics may be used to divide down the needed value of termination impedance. For example, ten of the filters in the fourth column of Table 3 can be hooked up in parallel to realize an R_Q=2000/10=200Ω. Note that the use of numerous filters in parallel also increases the power handling threshold. For example, if a given micromechanical filter were designed to handle 10 mW of power while retaining adequate linearity, then ten of them will handle 100 mW.

Once again, the ability to use of numerous high-*Q* elements in complex micromechanical circuits without regard to size greatly extends the applicable range of micromechanical signal processors. Given a suitable massive-scale trimming technique, the above parallel filter solution may work well even in the transmit path, perhaps making plausible some of the more aggressive power saving transmit architectures, such as that of Fig. 24.

6.4. Massive Scale Integration

Massive scale manufacturing technology capable of combining MEMS and transistor circuits onto single chips constitutes the fourth major research issue mentioned at the beginning of this section. The importance and breadth of this topic, however, demands a section of its own, which now follows.

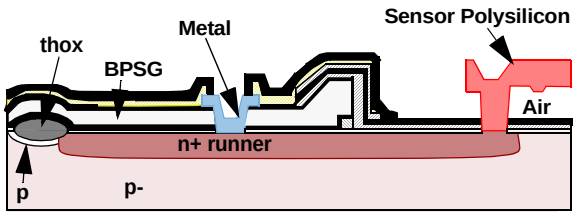

Fig. 28: Cross-section of the sensor area in Analog Devices' BiMOSII process [47].

7. Circuits/MEMS Integration Technologies

Although a two-chip solution that combines a MEMS chip with a transistor chip can certainly be used to interface μmechanical circuits with transistor circuits, such an approach becomes less practical as the number of μmechanical components increases. For instance, practical implementations of the switchable filter bank in Fig. 21 require multiplexing support electronics that must interconnect with each μmechanical device. If implemented using a two-chip approach, the number of chip-to-chip bonds required could become quite cumbersome, making a single-chip solution desirable.

In the pursuit of single-chip systems, several technologies that merge micromachining processes with those for integrated circuits have been developed and implemented over the past several years. These technologies can be categorized into three major approaches: mixed circuit and micromechanics, pre-circuits, and post-circuits. Each is now described.

7.1. Mixed Circuit and Micromechanics

In the mixed circuit/micromechanics approach, steps from both the circuit and the micromachining processes are intermingled into a single process flow. Of the three approaches, this one has so far seen the most use. However, it suffers from two major drawbacks: (1) many passivation layers are required (one needed virtually every time the process switches between circuits and μmechanics); and (2) extensive re-design of the process is often necessary if one of the combined technologies changes (e.g., a more advanced circuit process is introduced). Despite these drawbacks, mixed circuit/micromechanics processes have unquestionably made a sizable commercial impact. In particular, Analog Devices' BiMOSII process (Fig. 28 [47]), which has successfully produced a variety of accelerometers in large volume, is among the most successful examples of mixed circuit/micromechanics processes.

7.2. Pre-Circuits

In the pre-circuits approach, micromechanics are fabricated in a first module, then circuits are fabricated in a subsequent module, and no process steps from either module are intermingled. This process has a distinct advantage over the mixed process above in that advances in each module can be accommodated by merely replacing the appropriate module. Thus, if a more advanced circuit process becomes available, the whole merging process need not be re-designed; rather, only the circuits module need be replaced. An additional advantage is that only one passivation step is required after the micromechanics module.

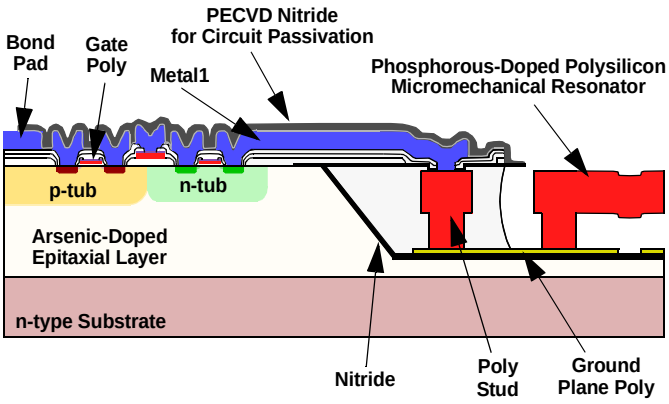

Fig. 29: Cross-section of Sandia's *iMEMS* process [48].

One of the main technological hurdles in implementing this process is the large topography leftover by micromechanical processes, with features that can be as high as 9 μm, depending upon the number and geometry of structural layers. Such topographies can make photoresist spinning and patterning quite difficult, especially if submicron circuit features are desired. These problems, however, have been overcome by researchers at Sandia National Laboratories, whose *iMEMS* process (Fig. 29) performs the micromechanics module in a trench, then planarizes features using chemical mechanical polishing (CMP) before doing the circuits module [48].

7.3. Post-Circuits

The post-circuit approach is the dual of pre-circuits, in which the circuits module comes first, followed by the micromechanics module, where again, no process steps from either module are interspersed. This process has all the advantages of pre-circuits, but with relaxed topography issues, since circuit topographies are generally much smaller than micromechanical ones. As a result, planarization is often not necessary before micromechanics processing. Post-circuit processes have the additional advantage in that they are more amenable to multi-facility processing, in which a very expensive fabrication facility (perhaps a foundry) is utilized for the circuits module, and relatively lower capital micromechanics processing is done in-house at the company site (perhaps a small start-up). Such an arrangement may be difficult to achieve with a pre-circuits process because IC foundries may not permit "dirty" micromachined wafers into their ultra-clean fabrication facilities.

Post-circuit processes have taken some time to develop. The main difficulty has been that aluminum based circuit metallization technologies cannot withstand subsequent high temperature processing required by many micromechanics processes—especially those that must achieve high Q. Thus, compromises in either the circuits process or the micromechanics process have been necessary, undermining the overall modularity of the process. The MICS process (Fig. 30 [17], [49]), which used tungsten metallization instead of aluminum to withstand the high temperatures used in a following polysilicon surface micromachining module, is a good example of a post-circuits process that compromises its metallization technology. More recent renditions of this process have now been introduced that retain aluminum metallization, while substituting lower temperature poly-SiGe as the structural material, with very little (if any) reduction in micromechanical performance [51].

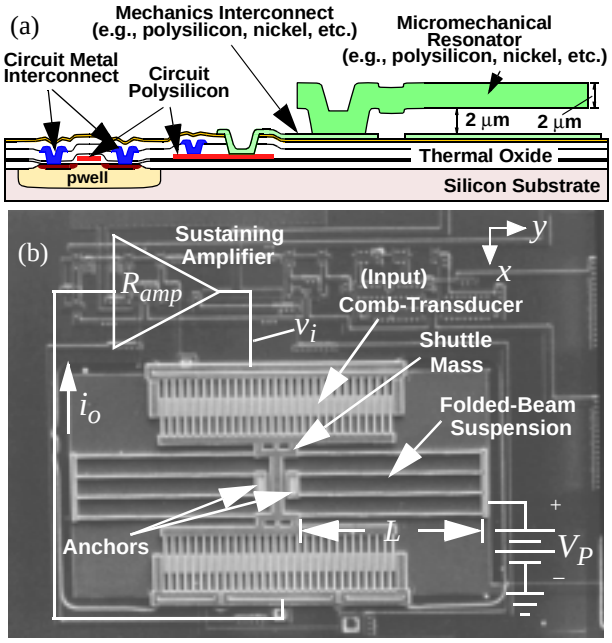

Fig. 30: (a) Cross-section of the MICS process [17]. (b) Overhead-view of a fully integrated micromechanical resonator oscillator fabricated using MICS [17].

7.4. Other Integration Approaches

There are number of other processes that can to some extent be placed in more than one of the above categories. These include front bulk-micromachining processes using deep reactive-ion etching (DRIE) [50] or anisotropic wet etchants [52] and other processes that slightly alter conventional CMOS processes [53]. In addition, bonding processes, in which circuits and μmechanics are merged by bonding one onto the wafer of the other, are presently undergoing a resurgence [54]. In particular, the advent of more sophisticated aligner-bonder instruments are now making possible much smaller bond pad sizes, which soon may enable wafer-level bonding with bond pad sizes small enough to compete with fully planar processed merging strategies in interface capacitance values. If the bond capacitance can indeed be lowered to this level with acceptable bonding yields, this technology may well be the ultimate in modularity.

From a cost perspective, which technology is best depends to a large extent on how much of the chip area is consumed by MEMS devices in the application in question. For cases where the MEMS utilizes only a small percentage of the chip area, bonding approaches may be more economical, since a larger number of MEMS chips can be achieved on a dedicated wafer. For cases where MEMS devices take up a large amount of chip area, or where node capacitance must be minimized for highest performance, planar integration may make more sense.

7.4.1. Vacuum Encapsulation

From a broader perspective, the integration techniques discussed above are really methods for achieving low capacitance packaging of microelectromechanical systems. From the discussion in Section 3.2, another level of packaging is required

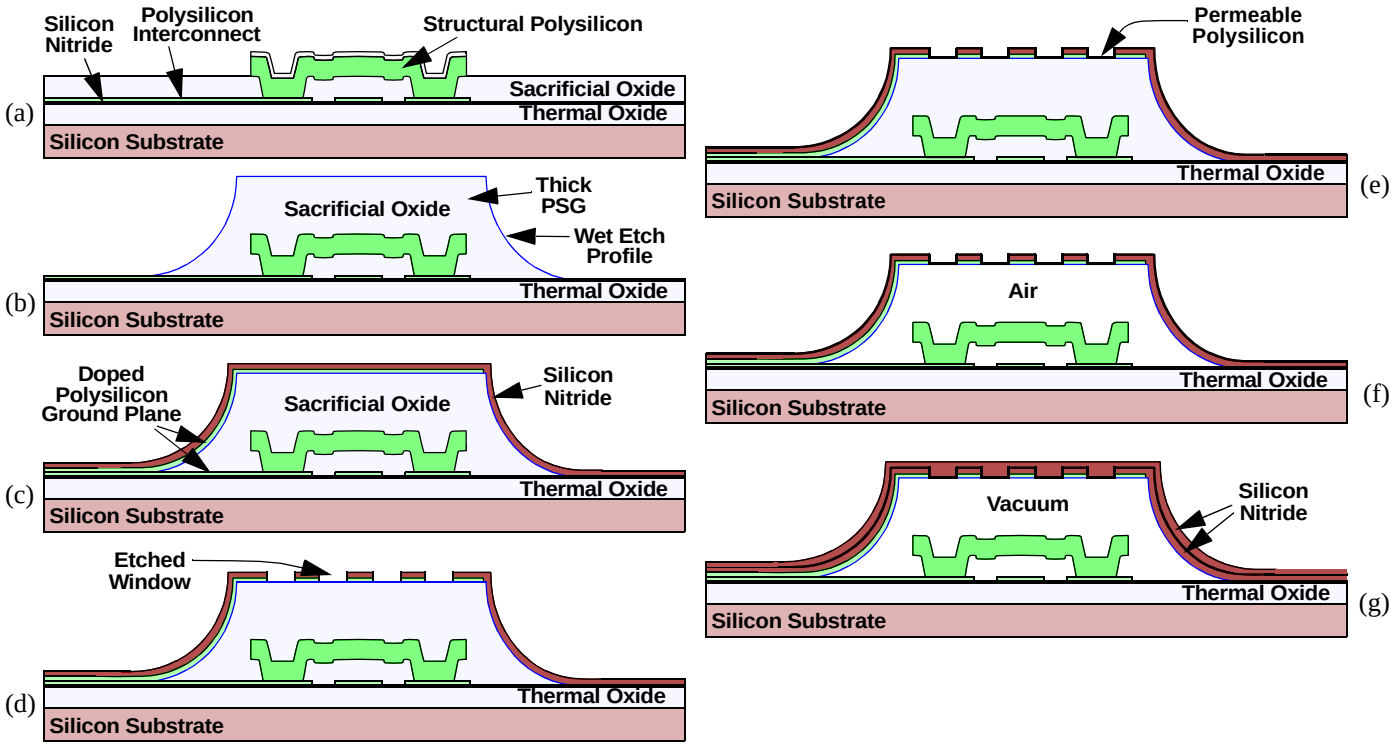

Fig. 31: Process flow for vacuum-encapsulating a micromechanical resonator via planar processing. (a) Cross-section immediately after the structural poly etch. (b) Deposit and pattern a thick, reflown PSG. (c) Deposit upper ground plane polysilicon and first nitride cap film. (d) Pattern etch windows in the cap. (e) Deposit permeable polysilicon [55]. (d) Etch sacrificial oxide (i.e., release structures) using HF, which accesses the sacrificial oxide through the permeable polysilicon, then dry via supercritical CO_2 [56], yielding the cross-section in (f). (g) Seal shell under vacuum via a second cap nitride deposition done in via LPCVD. Details for this process can be found in [55].

to attain high *Q* vibrating μmechanical resonators: vacuum encapsulation. Although the requirement for vacuum is unique to vibrating μmechanical resonators, the requirement for encapsulation is nearly universal for all of the micromechanical devices discussed in this paper. In particular, some protection from the environment is necessary, if only to prevent contamination by particles (or even by molecules), or to isolate the device from electric fields or feedthrough currents.

The need for encapsulation is, of course, not confined to communications devices, but also extends to the vast majority of micromechanical applications, e.g., inertial navigation sensors. For many micromechanical applications, the cost of the encapsulation package can be a significant (often dominating) percentage of the total cost of the product. Thus, to reduce cost, packaging technologies with the highest yield and largest throughput are most desirable. Pursuant to this philosophy, wafer-level packaging approaches—some based on planar processing, some based on bonding—have been the focus of much research in recent years. Figure 31 presents cross-sections that summarize one approach to *wafer-level* vacuum encapsulation [55], in which planar processing is used to realize an encapsulating cap. Although this and other encapsulation strategies have shown promise [57]-[60], there is still much room for improvement, especially given the large percentage of total product cost attributed to the package alone. Research to reduce the cost (i.e., enhance the yield and throughput) of encapsulation technologies continues.

8. Conclusions

Vibrating μmechanical resonators constitute the building blocks for a new integrated mechanical circuit technology in which high *Q* serves as a principal design parameter that enables more complex circuits. By combining the strengths of integrated μmechanical and transistor circuits, using both in massive quantities, previously unachievable functions become possible that enable transceiver architectures with projections for orders of magnitude performance gains. In particular, with the addition of high-*Q* μmechanical circuits, paradigm-shifting transceiver architectures that trade power for selectivity (i.e., *Q*) become possible, with the potential for substantial power savings and multi-band reconfigurability. To reap the benefits of these new architectures, however, further advancements in device frequency, linearity, and manufacturability are required. Research efforts are ongoing, and it is hoped that this chapter has provided enough background information and research foresight to instigate new efforts towards making mechanical circuits commonplace in the near future.

References

[1] H. Khorramabadi and P. R. Gray, "High-frequency CMOS continuous-time filters," *IEEE J. Solid-State Circuits*, vol. SC-19, No. 6, pp. 939-948, Dec. 1984.

[2] K. B. Ashby, I. A. Koullias, W. C. Finley, J. J. Bastek, and S. Moinian, "High *Q* inductors for wireless applications in a complementary silicon bipolar process," *IEEE J. Solid-State Circuits*, vol. 31, no. 1, pp. 4-9, Jan. 1996.

[3] N. M. Nguyen and R. G. Meyer, "Si IC-compatible inductors and *LC* passive filters," *IEEE J. of Solid-State Circuits*, vol. SC-25,

no. 4, pp. 1028-1031, Aug. 1990.

[4] P. R. Gray and R. G. Meyer, "Future directions in silicon IC's for RF personal communications," *Proceedings*, 1995 IEEE Custom Integrated Circuits Conference, Santa Clara, CA, May 1-4, 1995, pp. 83-90.

[5] R. A. Sykes, W. L. Smith, and W. J. Spencer, "Monolithic crystal filters," *1967 IEEE Int. Conv. Rec*., pt. II, March 20-23, 1967, pp. 78-93.

[6] R. C. Rennick, "An equivalent circuit approach to the design and analysis of monolithic crystal filters," *IEEE Trans. Sonics. Ultrasonc*., vol. SU-20, pp. 347-354, Oct. 1973.

[7] C. K. Campbell, *Surface Acoustic Wave Devices for Mobile Wireless Communications*. New York: Academic Press, Inc., 1998.

[8] C. T.-C. Nguyen, L. P.B. Katehi, and G. M. Rebeiz, "Micromachined devices for wireless communications (invited)," *Proc. IEEE*, vol. 86, no. 8, pp. 1756-1768, Aug. 1998.

[9] A. A. Abidi, "Direct-conversion radio transceivers for digital communications," *IEEE J. Solid-State Circuits*, vol. 30, No. 12, pp. 1399-1410, Dec. 1995.

[10] J. C. Rudell, J.-J. Ou, T. B. Cho, G. Chien, F. Brianti, J. A. Weldon, and P. R. Gray, "A 1.9-GHz wide-band IF double conversion CMOS receiver for cordless telephone applications," *IEEE J. Solid-State Circuits*, vol. 32, no. 12, pp. 2071-2088, Dec. 1997.

[11] K. Wang, Y. Yu, A.-C. Wong, and C. T.-C. Nguyen, "VHF free-free beam high-*Q* micromechanical resonators," *Technical Digest*, 12th Int. IEEE MEMS Conference, Orlando, Florida, Jan. 17-21, 1999, pp. 453-458.

[12] A. N. Cleland and M. L. Roukes, "Fabrication of high frequency nanometer scale mechanical resonators from bulk Si crystals," *Appl. Phys. Lett.*, **69** (18), pp. 2653-2655, Oct. 28, 1996.

[13] J. M. Bustillo, R. T. Howe, and R. S. Muller, "Surface micromachining for microelectromechanical systems," *Proc. IEEE*, vol. 86, no. 8, pp. 1552-1574, Aug. 1998.

[14] J. D. Cressler, et al., "Silicon-germanium heterojunction bipolar technology: the next leap for silicon?" *Digest of Technical Papers*, 1994 ISSCC, San Francisco, CA, February, 1994.

[15] N. Slawsby, "Frequency control requirements of radar," *Proceedings* of the 1994 IEEE International Frequency Control Symposium, June 1-3, 1994, pp. 633-640.

[16] W. P. Robins, *Phase Noise in Signal Sources*. London: Peter Peregrinus, Ltd., 1982.

[17] C. T.-C. Nguyen and R. T. Howe, "An integrated CMOS micromechanical resonator high-*Q* oscillator," *IEEE J. Solid-State Circuits*, vol. 34, no. 4, pp. 440-445, April 1999.

[18] F. D. Bannon, III, J. R. Clark, C. T.-C. Nguyen, "High-*Q* HF microelectromechanical filters," to be published in *IEEE J. Solid-State Circuits*, April 2000.

[19] K. M. Lakin, G. R. Kline, and K. T. McCarron, "Development of miniature filters for wireless applications," *IEEE Trans. Microwave Theory Tech.*, vol. 43, no. 12, pp. 2933-2939, Dec. 1995.

[20] S. V. Krishnaswamy, J. Rosenbaum, S. Horwitz, C. Yale, and R. A. Moore, "Compact FBAR filters offer low-loss performance," Microwaves & RF, pp. 127-136, Sept. 1991.

[21] R. Ruby and P. Merchant, "Micromachined thin film bulk acoustic resonators," *Proceedings* of the 1994 IEEE International Frequency Control Symposium, Boston, MA, June 1-3, 1994, pp. 135-138.

[22] W. E. Newell, "Miniaturization of tuning forks," *Science*, vol. 161, pp. 1320-1326, Sept. 1968.

[23] R. A. Johnson, *Mechanical Filters in Electronics*. New York: John Wiley & Sons, 1983.

[24] R. T. Howe and R. S. Muller, "Resonant microbridge vapor sensor," *IEEE Trans. Electron Device*s, ED-33, pp. 499-506, 1986.

[25] H. Nathanson, W. E. Newell, R. A. Wickstrom, and J. R. Davis, Jr., "The resonant gate transistor," *IEEE Trans. Electron Devices*, vol. ED-14, No. 3, pp. 117-133, March 1967.

[26] B. E. Boser and R. T. Howe, "Surface micromachined accelerometers," *IEEE J. of Solid-State Circuits*, vol. 31, no. 3, pp. 366-375, March 1996.

[27] N. Yazdi, F. Ayazi, K. Najafi, "Micromachined inertial sensors," *Proc. IEEE*, vol. 86, no. 8, pp. 1640-1659, Aug. 1998.

[28] H. A. C. Tilmans, "Equivalent circuit representation of electromechanical transducers: I. lumped-parameter systems," *J. Micromech. Microeng.*, 6, pp. 157-176 (1996).

[29] K. Wang and C. T.-C. Nguyen, "High-order medium frequency micromechanical electronic filters," *IEEE J. Microelectromech. Syst.*, vol. 8, no. 4, pp. 534-557, Dec. 1999.

[30] L. Lin, C. T.-C. Nguyen, R. T. Howe, and A. P. Pisano, "Micro electromechanical filters for signal processing," *Technical Digest*, IEEE Micro Electromechanical Systems Workshop, Travemunde, Germany, pp. 226-231, Feb. 4-7, 1992.

[31] A. I. Zverev, *Handbook of Filter Synthesis*. New York: John Wiley & Sons, 1967.

[32] P. R. Gray and R. G. Meyer, *Analysis and Design of Analog Integrated Circuits*, 2nd Ed. New York: John Wiley & Sons, 1984.

[33] M. S. Lee, "Polylithic crystal filters with loss poles at finite frequencies," *Proceedings*, 1975 IEEE Int. Symp. on Circuits and Syst., April 21-23, 1975, pp. 297-300.

[34] A.-C. Wong, H. Ding, and C. T.-C. Nguyen, "Micromechanical mixer+filters," *Technical Digest*, IEEE International Electron Devices Meeting, San Francisco, California, Dec. 6-9, 1998, pp. 471-474.

[35] C. Goldsmith, J. Randall, S. Eshelman, T. H. Lin, D. Denniston, S. Chen and B. Norvell, "Characteristics of micromachined switches at microwave frequencies," IEEE MTT-S Digest, pp. 1141-1144, June, 1996.

[36] D. J. Young and B. E. Boser, "A micromachined variable capacitor for monolithic low-noise VCOs," *Technical Digest*, 1996 Solid-State Sensor and Actuator Workshop, Hilton Head Island, South Carolina, June 3-6, 1996, pp. 86-89.

[37] W. Y. Ali-Ahmad, "RF system issues related to CDMA receiver specifications," *RF Design*, pp. 22-32, Sept. 1999.

[38] D. K. Shaeffer and T. H. Lee, "A 1.5-V, 1.5-GHz CMOS low noise amplifier," *IEEE J. Solid-State Circuits*, vol. 32, No. 5, pp. 745-759, May 1997.

[39] R. G. Meyer and A. K. Wong, "Blocking and desensitization in RF amplifiers," *IEEE J. Solid-State Circuits*, vol. 30, No. 8, pp. 994-946, Aug. 1995.

[40] D. B. Leeson, "A simple model of feedback oscillator noise spectrum," *Proc. IEEE*, vol. 54, pp. 329-330, Feb. 1966.

[41] J. F. Parker and D. Ray, "A 1.6-GHz CMOS PLL with on-chip loop filter," *IEEE J. Solid-State Circuits*, vol. 33, no. 3, pp. 337-343, March 1998.

[42] P. Orsatti, F. Piazza, and Q. Huang, "A 70-MHz CMOS IF-baseband strip for GSM," *IEEE J. Solid-State Circuits*, vol. 35, No. 1, pp. 104-108, Jan. 2000.

[43] V. B. Braginskky, V. P. Mitrofanov, and V. I. Panov, *Systems With Small Dissipation*. Chicago: University of Chicago Press., 1985.

[44] F. D. Bannon III and C. T.-C. Nguyen, "High frequency microelectromechanical IF filters," *Technical Digest*, 1996 IEEE Electron Devices Meeting, San Francisco, CA, Dec. 8-11, 1996, pp. 773-776.

[45] K. Wang and C. T.-C. Nguyen, "High-order micromechanical electronic filters," *Proceedings*, 1997 IEEE International Micro Electro Mechanical Systems Workshop, Nagoya, Japan, Jan. 26-30, 1997, pp. 25-30.

[46] K. Wang, A.-C. Wong, W.-T. Hsu, and C. T.-C. Nguyen, "Frequency-trimming and *Q*-factor enhancement of micromechanical resonators via localized filament annealing," *Digest of Technical Papers*, 1997 International Conference on Solid-State Sensors and Actuators, Chicago, Illinois, June 16-19, 1997, pp. 109-112.

[47] T. A. Core, W. K. Tsang, S. J. Sherman, "Fabrication technology for an integrated surface-micromachined sensor," *Solid State Technology*, pp. 39-47, Oct. 1993.

[48] J. H. Smith, S. Montague, J. J. Sniegowski, J. R. Murray, *et al*., "Embedded micromechanical devices for the monolithic integration of MEMS with CMOS," *Proceedings*, IEEE International Electron Devices Meeting, Washington, D.C., Dec. 10-13, 1995, pp. 609-612.

[49] J. M. Bustillo, G. K. Fedder, C. T.-C. Nguyen, and R. T. Howe, "Process technology for the modular integration of CMOS and polysilicon microstructures," *Microsystem Technologies*, **1**

(1994), pp. 30-41.

[50] T. J. Brosnihan, J. M. Bustillo, A. P. Pisano, and R. T. Howe, "Embedded interconnect and electrical isolation for high-aspect-ratio SOI inertial instruments," *Digest of Technical Papers*, 1997 International Conference on Solid-State Sensors and Actuators, Chicago, Illinois, June 16-19, 1997, pp. 637-640.

[51] A. E. Franke, D. Bilic, D. T. Chang, P. T. Jones, T.-J. King, R. T. Howe, and G. C. Johnson, "Post-CMOS integration of germanium microstructures," *Technical Digest*, 12th Int. IEEE MEMS Conf., Orlando, Florida, Jan. 17-21, 1999, pp. 630-637.

[52] H. Baltes, O. Paul, and O. Brand, "Micromachined thermally based CMOS microsensors," *Proc. IEEE*, vol. 86, no. 8, pp. 1660-1678, Aug. 1998.

[53] G. K. Fedder, S. Santhanam, M. L. Reed, S. C. Eagle, D. F. Guillou, M. S.-C. Lu, and L. R. Carley, "Laminated high-aspect-ratio microstructures in a conventional CMOS process," *Sensors and Actuators*, vol. A57, no. 2, pp. 103-110, March 1997.

[54] A. Singh, D. A. Horsley, M. B. Cohn, A. P. Pisano, and R. T. Howe, "Batch transfer of microstructures using flip-chip solder bonding," *J. Microelectromech. Syst.*, vol. 8, no. 1, pp. 27-33, March 1999.

[55] K. S. Lebouitz, A. Mazaheri, R. T. Howe, and A. P. Pisano, "Vacuum encapsulation of resonant devices using permeable polysilicon," *Technical Digest*, 12th International IEEE MEMS Conference, Orlando, Florida, Jan. 17-21, 1999, pp. 470-475.

[56] G. T. Mulhern, D. S. Soane, and R. T. Howe, "Supercritical carbon dioxide drying of microstructures," 7th International Conference on Solid-State Sensors and Actuators (Transducers'93), Yokohama, Japan, June 1993, pp. 296-299.

[57] R. Legtenberg and H. A. C. Tilmans, "Electrostatically driven vacuum-encapsulated polysilicon resonators," *Sensors and Actuators*, vol. A45, pp. 57-66 (1994).

[58] L. Lin, K. M. McNair, R. T. Howe, and A. P. Pisano, "Vacuum-encapsulated lateral microresonators," *Digest of Technical Papers*, the 7th International Conference on Solid-State Sensors and Actuators (Transducers'93), Yokohama, Japan, June 7-10, 1993, pp. 270-273.

[59] M. B. Cohn, Y. Liang, R. T. Howe, and A. P. Pisano, "Wafer-to-wafer transfer of microstructures for vacuum packaging," *Technical Digest*, Solid-State Sensor and Actuator Workshop, Hilton Head Island, South Carolina, June 3-6, 1996, pp. 32-35.

[60] S. Mack, H. Baumann, and U. Gosele, "Gas tightness of cavities sealed by silicon wafer bonding," *Proceedings*, 10th Int. Workshop on Micro Electro Mechanical Systems, Nagoya, Japan, Jan. 26-30, 1997, pp. 488-493.